Table of contents

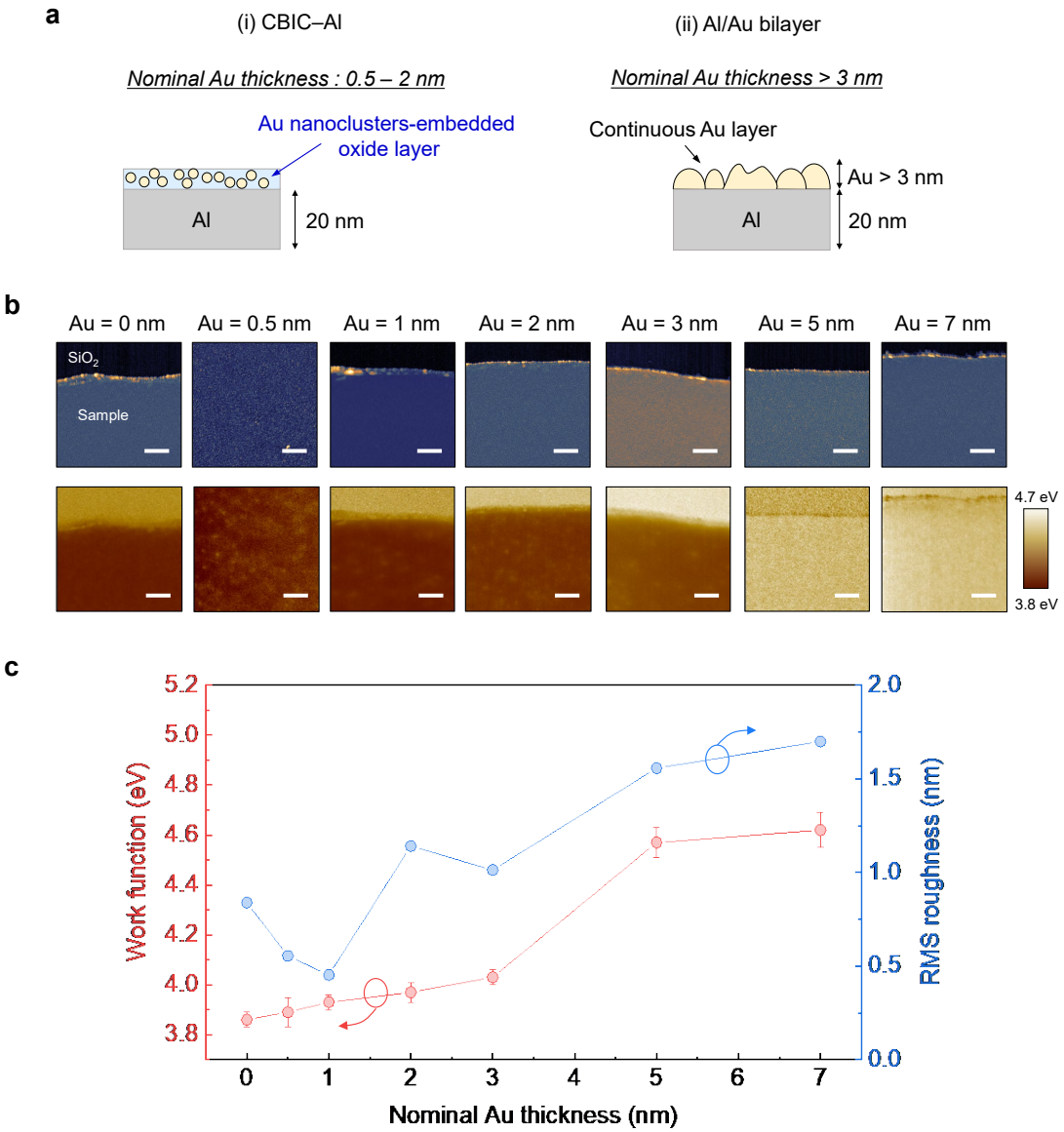

Supplementary Fig. 1. Characterizations of CBIC–Al with different nominal Au thicknesses. a, Schematic of two different contact structures: (i) Conductive-bridge interlayer contact (CBIC)–Al and (ii) Al/Au metal bilayer. **b,** AFM topology images (top row) and corresponding KPFM images (bottom row) of the samples. Scale bars, 1 μm. **c,** Work function and root mean square (RMS) roughness variation of the samples as a function of nominal Au thickness. All error bars represent the standard deviation for each case.

To ensure reliable CBIC fabrication and integration with two-dimensional (2D) materials, it

is essential to maintain the atomic smoothness of the CBIC and preserve the work function of the pristine metals (Al, Ti, Cr, and Cu). To this end, we extensively characterized the surface and work function of CBIC–Al with different nominal Au thicknesses. (In this study, the Au content was precisely controlled by the nominal thickness of Au during the subsequent sputtering process.) From topographical AFM images (top row of Fig. S1b), the 1-nm-thick Au CBIC–Al shows a smooth surface with RMS roughness of 0.45 nm (over an area of 2×2 μm^2). Increasing the Au thickness resulted in a rougher surface, mainly due to the formation of isolated Au islands or percolated networks, leading to an increased RMS roughness of 1 to 1.5 nm.

Meanwhile, CBIC–Al samples with varying Au thicknesses exhibit distinctly different work functions in KPFM images (bottom row of Fig. S1b). As the nominal Au thickness increases, the work function increases from 3.86 ± 0.03 eV (Au = 0 nm) to 4.62 ± 0.07 eV (Au = 7 nm). Notably, there is a drastic change in the work function values between 3 nm and 5 nm Au thickness. We attribute this to the fact that when the nominal Au thickness exceeds 3 nm, a continuous Au layer tends to form on Al [illustrated in Fig. S1a(ii)], resulting in a work function approaching that of bulk Au. In contrast, trace amounts of Au (nominal Au thickness less than 3 nm) can form Au nanoclusters embedded in the oxide interlayer [illustrated in Fig. S1a(i)], as expected. In this case, the work function of the CBIC is largely determined by the underlying deposited metal (*i.e.*, Al), as also confirmed by KPFM measurements (Fig. 2b in the main text). Considering these two aspects (work function and surface roughness), we therefore determined the optimal Au thickness to be approximately 1 nm.

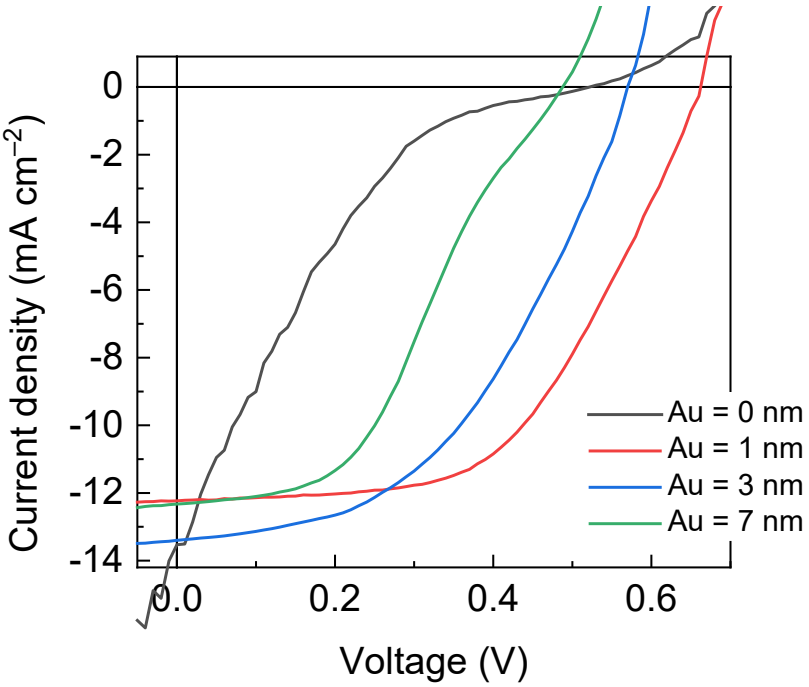

Devices	V_{OC} (V)	J_{SC} (mA cm^{-2})	FF (%)	PCE (%)	R_S (MΩ)	R_{SH} (GΩ)
Au = 0 nm	0.52	13.54	14	2.24	181	0.02
Au = 1 nm	0.66	12.23	54	9.91	4.84	0.8
Au = 3 nm	0.57	13.40	47	8.16	4.67	0.17
Au = 7 nm	0.49	12.33	41	5.63	10.4	0.21

Supplementary Fig. 2. *J*–*V* curves of CBIC–Al devices with different nominal Au thicknesses, measured under light illumination (532 nm, 44 mW cm^{-2}). The table shows the performance parameters of the corresponding devices.

We have investigated the dependence of the nominal Au thickness on the CBIC–Al device parameters (V_{OC}, J_{SC}, FF, PCE, R_S, and R_{SH}). Fig. S2 reveals that the optimal Au thickness for device performance (that is, the highest PCE) is approximately 1 nm. With increased Au thickness, the devices tend to exhibit an s-shaped curve with higher series resistance (R_S), which can be largely attributed to an increased contact barrier for charge extraction[1]. This implies that CBICs with thicker Au exhibit surface properties similar to those of pristine Au metal, potentially leading to a larger contact barrier for electron extraction.

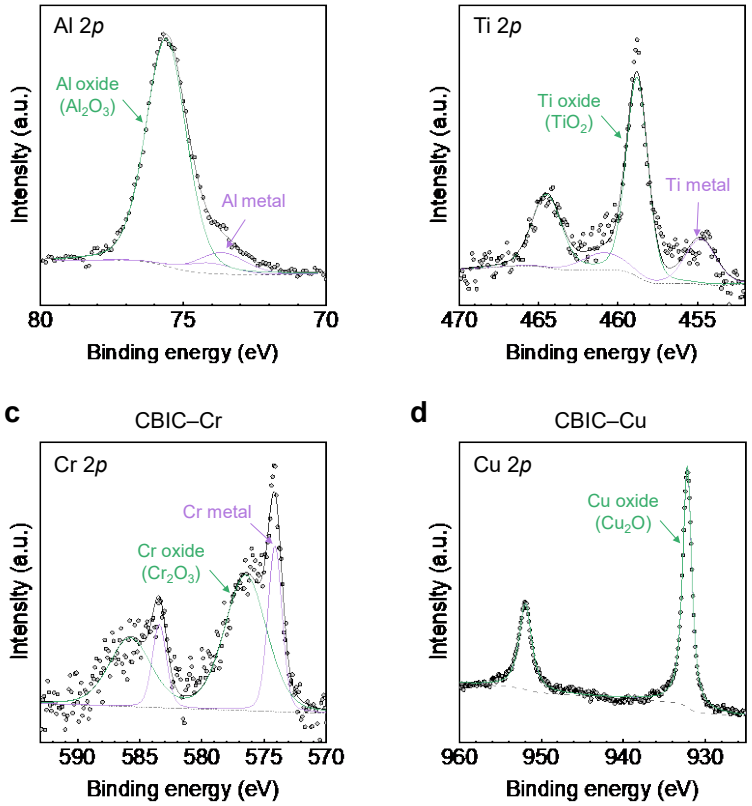

Supplementary Fig. 3. X-ray photoelectron spectroscopy (XPS) characterization of the CBIC. a–d, XPS spectra of the 2*p* core level for CBIC–Al (**a**), Ti (**b**), Cr (**c**), and Cu (**d**). The XPS spectra show the coexistence of characteristic metal peaks with oxidation states. This indicates that the surface of low-WF metals is successfully converted to native oxide layers, while the rest of the metal remains pristine.

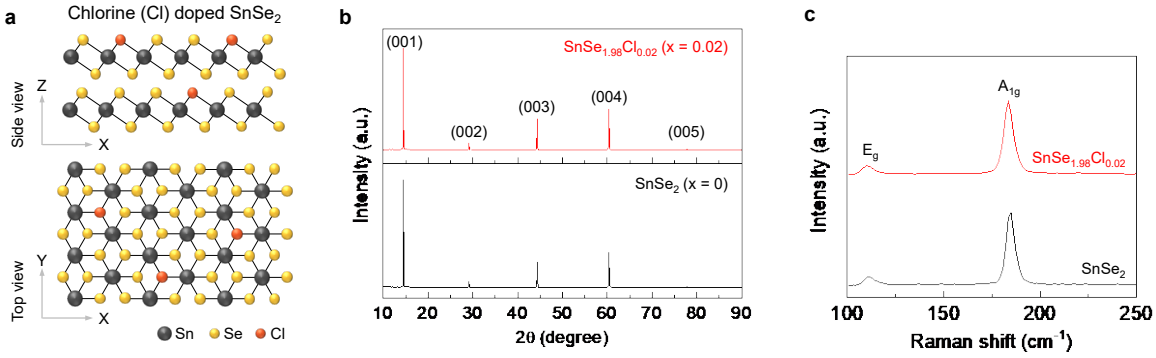

Supplementary Fig. 4. Characterization of the Cl–$SnSe_2$ used in this study. a, Schematic crystal structure of Cl–$SnSe_2$. **b,** XRD measurement results of Cl–$SnSe_2$ (red) and undoped $SnSe_2$ (black). The identical peak positions observed in Cl–$SnSe_2$ and the undoped $SnSe_2$ indicate that good crystallinity is preserved in Cl–$SnSe_2$ without the formation of non-stoichiometric structures. **c,** Raman spectra of Cl–$SnSe_2$ (red) and undoped $SnSe_2$ (black).

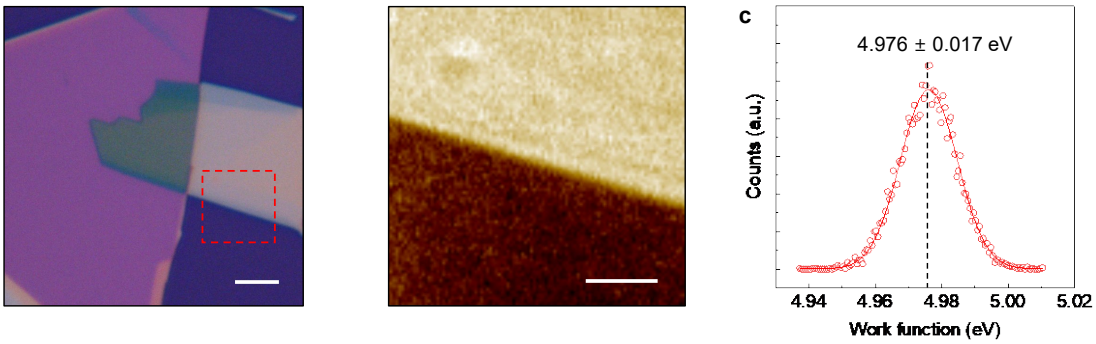

Supplementary Fig. 5. KPFM measurement of Cl–$SnSe_2$. a, Optical image of the WS_2/Cl–$SnSe_2$ heterostructure. **b,** KPFM work function mapping image of the area highlighted with the dashed square in **a**. **c,** Work function distribution of Cl–$SnSe_2$. The work function of Cl–$SnSe_2$ was measured to be ~4.98 eV, similar to previously reported values[2,3].

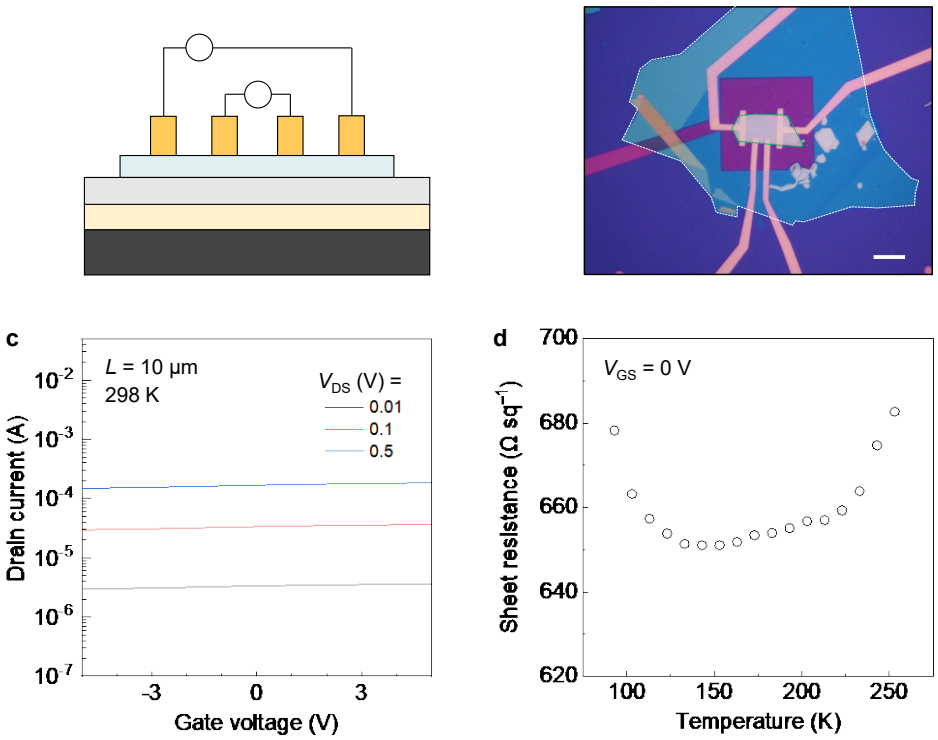

Supplementary Fig. 6. Electrical measurement of the Cl–$SnSe_2$ device. a, Schematic of the ~13 nm thick Cl–$SnSe_2$ four-terminal device consisting of two outer probes and two inner probes. **b,** Optical image of the device. **c,** Transfer characteristics of the device. Negligible gate modulation at a high current level demonstrates the metallicity of Cl–$SnSe_2$. **d,** Sheet resistance as a function of temperature. A metal–insulator transition is observed at ~140 K[4]. Furthermore, sheet resistance increases with temperature from 140 to 250 K, which is a clear indication of the metallic characteristic of Cl–$SnSe_2$.

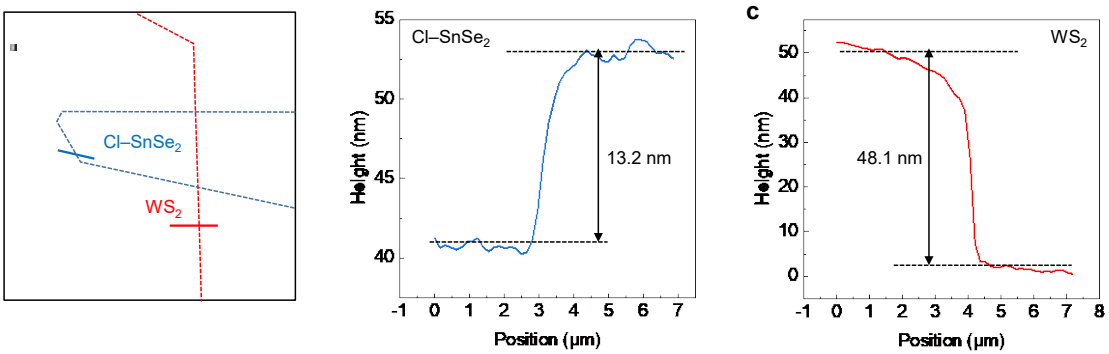

Supplementary Fig. 7. AFM measurement of the complete device. a, AFM height image of the device (the same sample as shown in Fig. 1c in the main text). **b,c,** Height profiles of Cl–$SnSe_2$ (**b**) and WS_2 (**c**) layers taken from the blue and red solid lines in **a**, indicating thicknesses of approximately 13.2 and 48.1 nm, respectively.

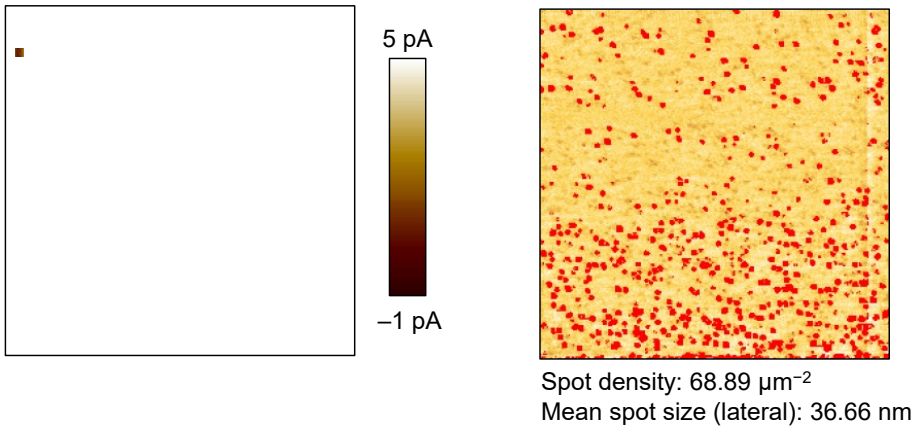

Supplementary Fig. 8. Statistical analysis of conductive spots in CBIC−Al. a, Conductive atomic force microscopy (CAFM) current map (left) of CBIC−Al and corresponding statistical analysis (right) using Park Systems XEI software for image processing and analysis.

From statistical analysis (Fig. S8), the density of the conductive spots was approximately 68.69 μm^{-2}. The lateral size of the conductive spots was measured to be approximately 36.66 nm; however, this value may be overestimated due to the shape of the conductive atomic force microscopy (CAFM) tip. It is known that the CAFM measurement conditions, including tip radius, tip coating, contact force, and applied bias, can have a significant impact on the results. Given that the tip radius here was < 25 nm, the actual size of the conductive spots can be estimated to be approximately 10 nm, consistent with the conductive paths observed in the STEM image (Fig. S9).

The primary goal of the CAFM measurement was to reveal the spatial distribution of the conductive paths in CBIC–Al rather than to perform a quantitative estimation of the current passing through these paths. As mentioned above, experimental conditions can significantly influence the current measurement via CAFM. Therefore, the particular measured current value in a conductive path, whether it is (for example) 5 pA or 50 pA, is not of importance in the present study. In addition, the absence of WS_2 and Cl–$SnSe_2$ layers in our CAFM sample,

which significantly differs from the structure of the complete devices, may also complicate the measurement of accurate current values.

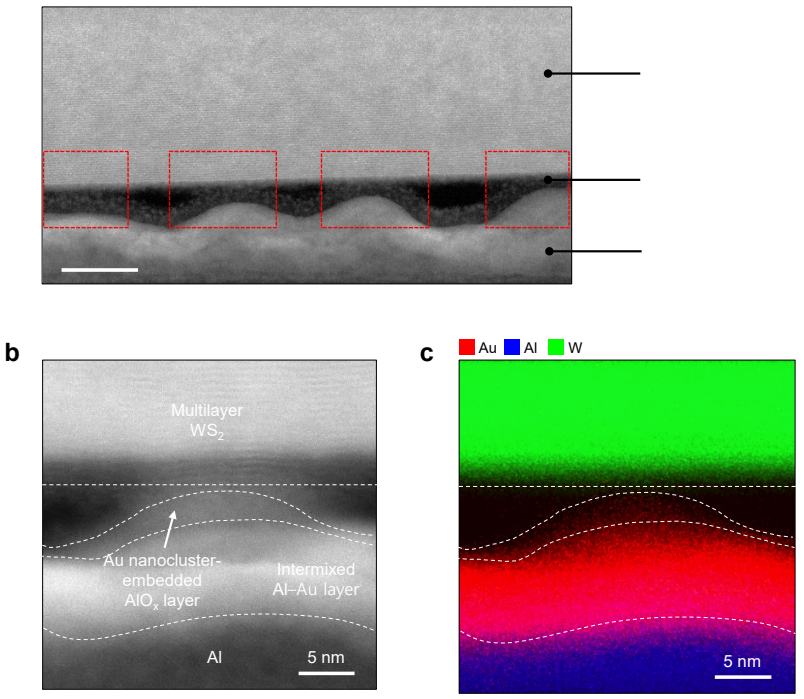

Supplementary Fig. 9. Cross-sectional STEM and energy-dispersive X-ray spectroscopy (EDS) analysis of the WS_2 device with CBIC–Al contact. a, Low-magnification cross-sectional STEM image of the complete device. The bright spots along the bottom WS_2 layer might be residual WS_2 particles due to focused ion beam damage. **b,** Enlarged STEM image of the CBIC–Al/WS_2 interface. **c,** Corresponding EDS mapping image, revealing a spatially uniform distribution of Au within the AlO_x layer.

Numerous intimate junctions between WS_2 and CBIC–Al are clearly observed (red dashed squares in Fig. S9a), where the distances between them are from ~40 nm to ~100 nm, consistent with the CAFM results (Fig. S8). In fact, relatively large distances between the junctions are an unfavorable feature of the device because they may deteriorate the reproducibility of the CBIC properties and pose a scaling limit for nanoscale devices. Large gaps between junctions are largely due to the protrusion morphology of the underlying metal and can be reduced with a more controlled metal deposition process.

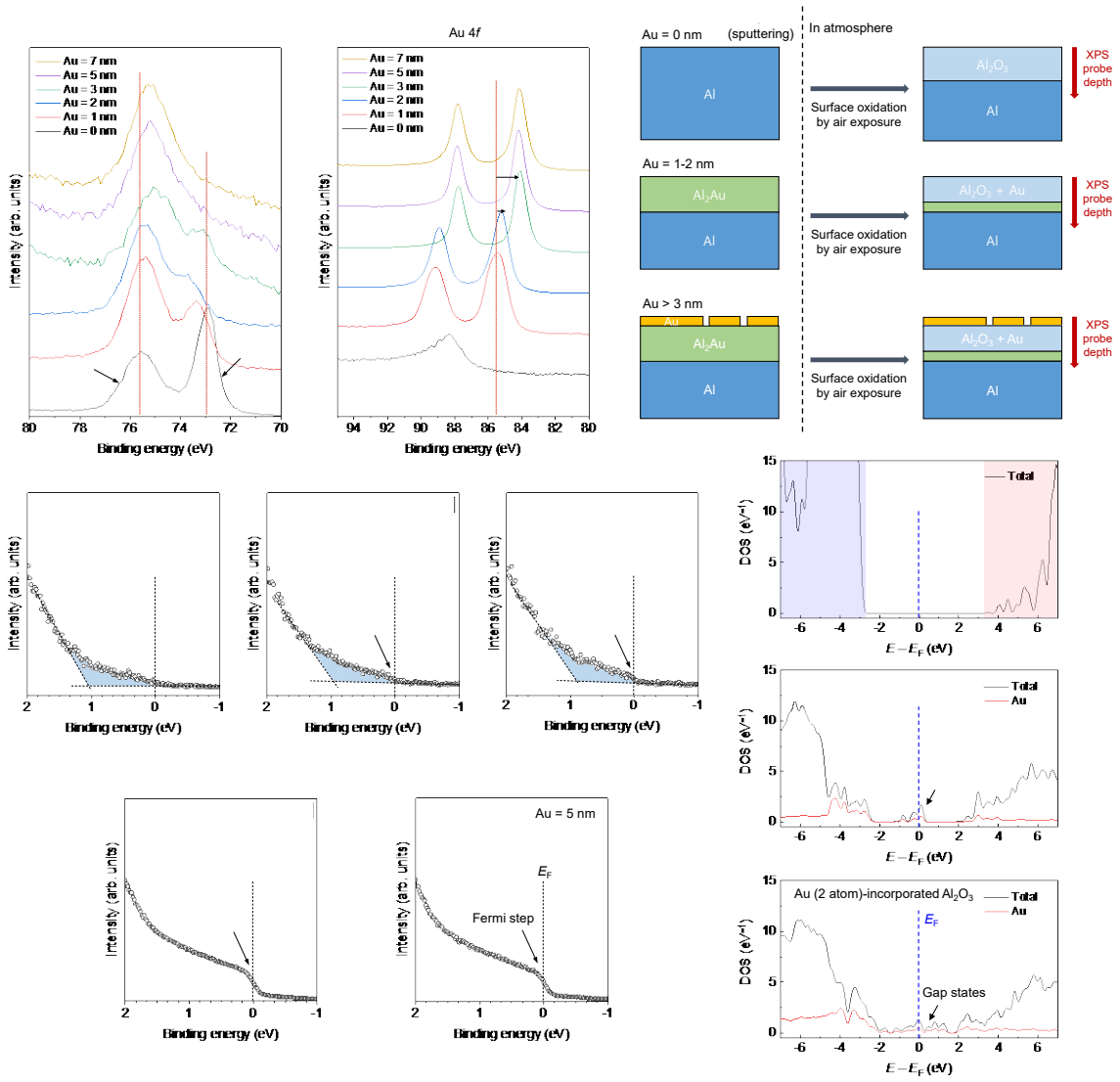

Supplementary Fig. 10. Conduction mechanism in CBIC–Al. a, XPS spectra of CBIC–Al as a function of nominal Au thickness. **b,** Schematic illustrations of CBIC–Al samples with different Au thicknesses. **c,** Valence band spectra of the same samples. **d,** Density of states (DOS) of α-Al_2O_3 interlayer models with a varying number of elemental Au atoms, showing the evolution of gap states within the bandgap. The gap states near the Fermi level (E_F) may contribute to electrical conduction across the interlayer.

To clarify the conduction mechanism of the CBIC, we systematically performed XPS measurements to characterize the chemistry of the CBIC–Al samples. The Al 2*p* spectra for

CBIC–Al samples with different nominal Au thicknesses are shown in Fig. S10a. For the sample with Au = 0 nm, the binding energy values for the Al 2*p* doublets were found to be 75.6 and 72.9 eV, which are typical of naturally oxidized Al film[5]. For the Au = 1 nm sample, the data can be resolved into two component peaks at binding energies of 75.4 and 73.4 eV. The 75.4 eV peak matches well with the reported binding energy of oxidic Al, and thus this can be identified as Al_2O_3. The other peak at 73.4 eV originates from the metallic Al species in Al_2Au[5,6], and its intensity gradually reduced as the Au thickness increased. The corresponding XPS spectra of the Au 4*f* region is also shown in Fig. S10a. Two components of the Au peak are clearly visible, with binding energies of 89.1 eV (Au $4f_{5/2}$) and 85.5 eV (Au $4f_{7/2}$), evidencing the formation of the Al_2Au phase[5,7] in CBIC–Al. Further increase of Au thickness should practically lead to a Au thin film, as confirmed by the clear shift in the Au $4f_{7/2}$ peak to 84.0 eV (corresponding to metallic Au[8]). Taken together, these experimental observations demonstrate the formation of an Al_2Au intermetallic layer. It is well known that Al_2Au readily forms at Al/Au interfaces at room temperature[5].

Most importantly, such an Al_2Au intermetallic layer can transform to Au upon exposure to ambient air at room temperature, a phenomenon previously demonstrated in Al–Au thin film alloys[5]. This principle is consistent with our observations on the CBIC–Al samples. This reaction can be described by:

$$2Al_2Au + 3O_2 \rightarrow 2Al_2O_3 + 2Au$$

By uniform oxidation, a homogeneous and nanometer-thick native oxide layer (Al_2O_3) can be formed, where Au exists in the form of solute atoms and/or nanoclusters. This is in good agreement with our experimental TEM and EDS results (Fig. 1h,i in the main text and Fig. S9b,c), and can be schematically illustrated in Fig. S10b. At this point, we can find no satisfactory explanation for the formation of these nanoclusters; further studies on the activation energy of these nanoclusters are needed to fully understand their formation

mechanism. The reduced series resistance of interlayer contacts is fundamentally based on the embedded Au atoms within the oxide layer: the dissolution of noble Au metals within the oxide interlayer reduces the conductivity loss caused by the oxide, which is of great significance for reducing the series resistance of contacts.

Moreover, to investigate whether electronic properties (such as the formation of gap states within the bandgap) are responsible for the low resistance of CBIC–Al, the valence band structure of the same samples was also investigated, as shown in Fig. S10c. Starting with curve Au = 0 nm, there is a clear trend showing that increasing the nominal Au thickness leads to an increment in the density of gap states near the Fermi level, approaching a metallic system similar to the case of Au film (as evidenced by the steplike intensity at the Fermi level in the samples with 2–7 nm Au thickness). Therefore, we conclude that the elemental Au is likely responsible for the increased gap states. To corroborate this interpretation, density functional theory (DFT) calculations were also performed. As depicted in Fig. S10d, projections of Au states onto the Al_2O_3 bandgap are clearly noticeable, indicating that coupling between elemental Au atoms and the Al_2O_3 layer leads to the formation of gap states within the bandgap. Thus, unoccupied gap states near the Fermi level may contribute to efficient charge-carrier transport through the interlayer, which could be responsible for the observed enhanced conductance in CBIC–Al.

In the DFT calculations, an α-Al_2O_3 slab with various supercells, was selected for computational modelling. All DFT calculations were performed using the plane-wave pseudopotential code Quantum Espresso[9], and the Perdew–Burke–Ernzerhof (PBE) general gradient approximation was used to describe exchange-correlation effects[10]. The electronic wavefunctions were expanded in a plane-wave basis with a cutoff of 25 Ry and charge-density cutoff of 255 Ry. In all calculations, all atomic positions (Al, O, and Au) were relaxed until the

forces were less than 0.01 eV $Å^{-6}$. The convergence threshold used for total energy was 1×10^{-6} eV. A *k*-point mesh of 12 × 12 × 1 was used.

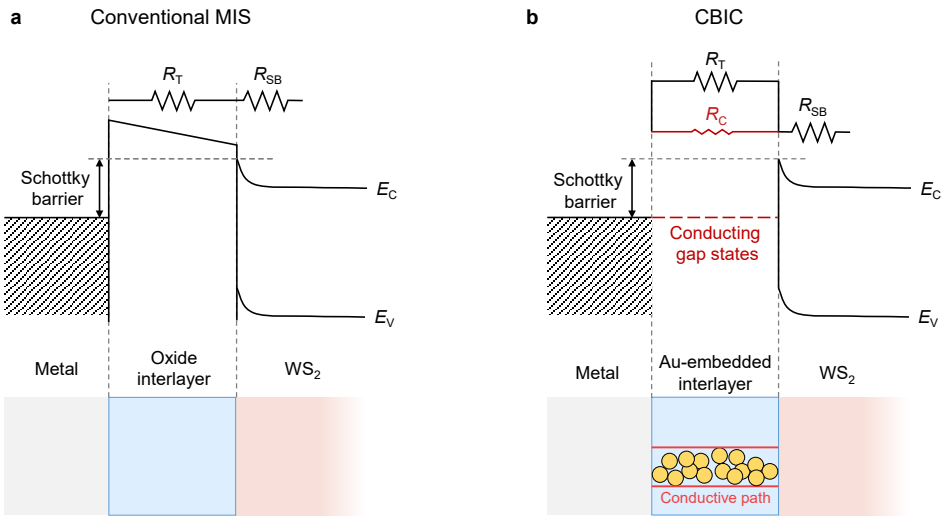

Supplementary Fig. 11. Charge transport mechanism of the CBIC. a,b, Device structure and schematic band diagrams of a conventional metal–interlayer–semiconductor (MIS) contact (**a**) and the CBIC (**b**). R_T, R_{SB}, and R_C represent tunnelling resistance, Schottky barrier resistance, and conductive path resistance, respectively.

In general, the total resistance of a conventional metal–interlayer–semiconductor (MIS) contact can be described by two components in series: (i) the Schottky barrier resistance (R_{SB}), which depends on the Schottky barrier height at the metal−semiconductor junction, and (ii) the tunnelling resistance (R_T), which depends on the tunnelling barrier formed by the interlayer[12]. The optimal interlayer thickness is determined by a trade-off between the decrease in R_{SB} and increase in R_T with increasing interlayer thickness. This principle is also consistent with the MIS contact studied in this work. In the MIS contact structure (Fig. S11a), with a thin oxide interlayer, Fermi level unpinning can significantly decrease the Schottky barrier height, leading to a substantial reduction in R_{SB}. However, the oxide interlayer can also introduce a notable tunnelling resistance (R_T). This tunnelling resistance effect becomes more pronounced as the interlayer thickness exceeds its optimal value (typically around 1 nm), resulting in increased

overall contact resistance despite the low Schottky barrier height. By contrast, in the CBIC structure (Fig. S11b), current can flow mostly through the Au atom bridges in the conducting state without compromising the tunnelling resistance induced by the interlayer.

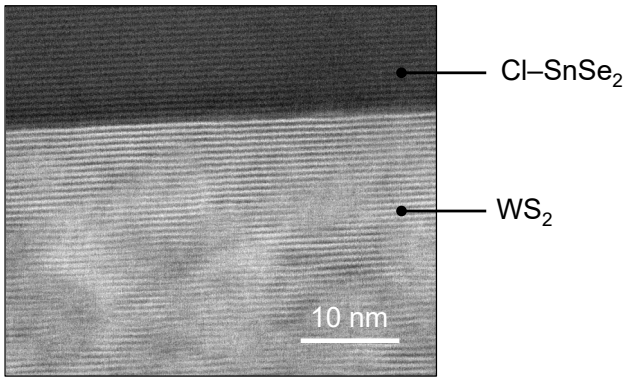

Supplementary Fig. 12. Low-magnification cross-sectional STEM image of WS_2 with Cl–$SnSe_2$. The Cl–$SnSe_2$/WS_2 interface features atomically clean contact without any apparent interfacial defects.

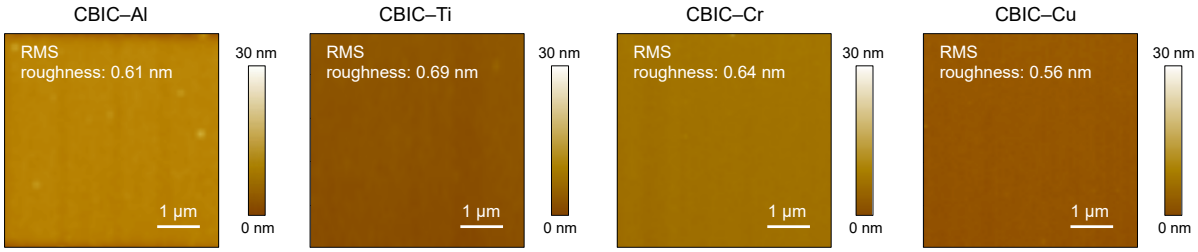

Supplementary Fig. 13. AFM topology images of various CBIC electrodes. All CBIC electrodes demonstrate a smooth surface with RMS roughness of 0.56–0.69 nm. Note that the surface roughness of the resulting electrodes is largely dictated by the morphology of the underlying base metals (Al, Ti, Cr, and Cu) and/or the uneven substrate caused by residual polymers and any other contaminants. Roughness can be reduced with a more controlled metallization and cleaning process (*e.g.*, O_2 plasma ashing to remove contaminants).

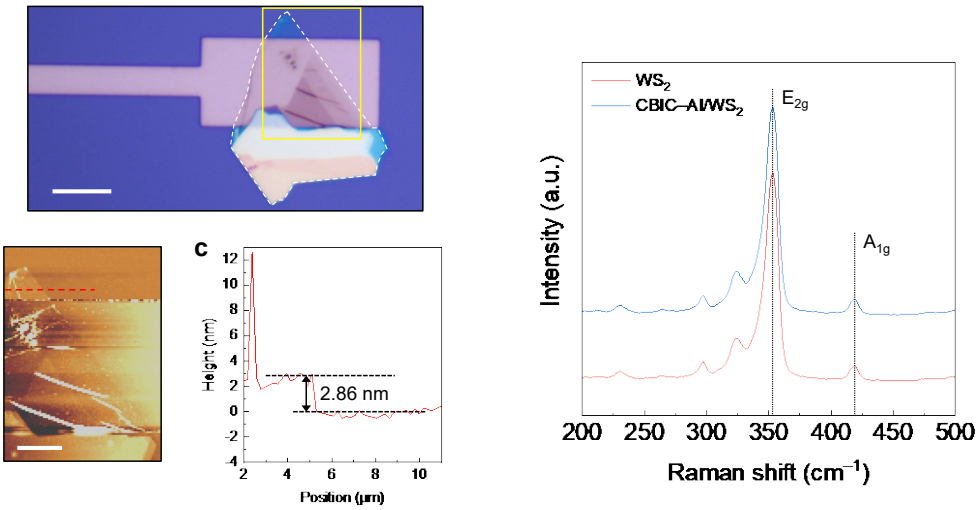

Supplementary Fig. 14. CBIC–Al/WS_2 heterostructure sample for XPS and Raman analysis. a, Optical image of the CBIC–Al/WS_2 heterostructure sample for XPS and Raman analysis. **b,** AFM height image highlighted with yellow square in **a**. **c,** Height profile along the dashed line in **b**. **d,** Raman spectra of WS_2 (red) and the CBIC–Al/WS_2 (blue) using an excitation wavelength of 532 nm. We intentionally prepared the sample using thin WS_2 (~2.86 nm, four layers) to ensure a reliable evaluation of interfacial chemistry between WS_2 and CBIC–Al. The Raman data clearly show in-plane E_{2g} and out-of-plane A_{1g} modes for the CBIC–Al/WS_2 structure with no evidence for non-stoichiometric W_xS_y, indicating that the structural integrity of pristine WS_2 was maintained after the CBIC–Al integration process.

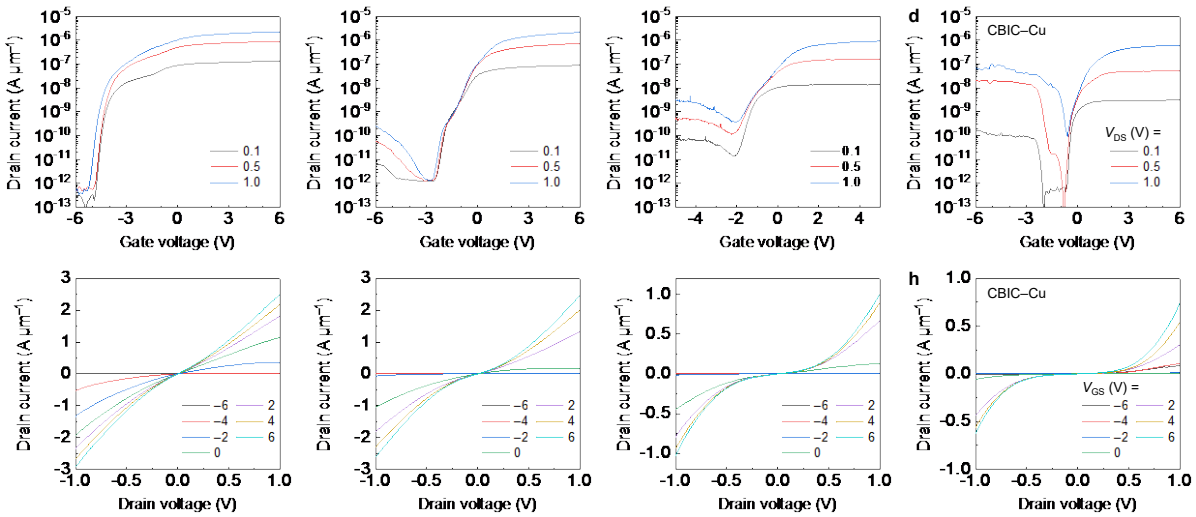

Supplementary Fig. 15. Top-gated multilayer WS_2 transistors with various CBIC electrodes. a–d, Room temperature transfer characteristics of the device with CBIC–Al (**a**), Ti (**b**), Cr (**c**), and Cu (**d**), the same devices as in Fig. 2e–h in the main text. **e–h,** Corresponding output characteristics at different gate voltages (V_{GS}).

We fabricated multilayer WS_2 transistors with different types of CBIC electrodes. We found that the carrier polarity of the devices is strongly dependent on the work functions of the CBICs, demonstrating a switching from n-type to ambipolar transport, consistent with a previous report[13]. For example, for CBIC–Al electrodes with a low work function ($W \approx 3.92$ eV), the n-type characteristic was observed, indicating that a low electron barrier was formed. With an increase in metal work function by using CBIC–Cu electrodes ($W \approx 4.74$ eV), the device clearly exhibited ambipolar behaviour. These results suggest that Fermi level unpinning can be achieved with our CBIC method.

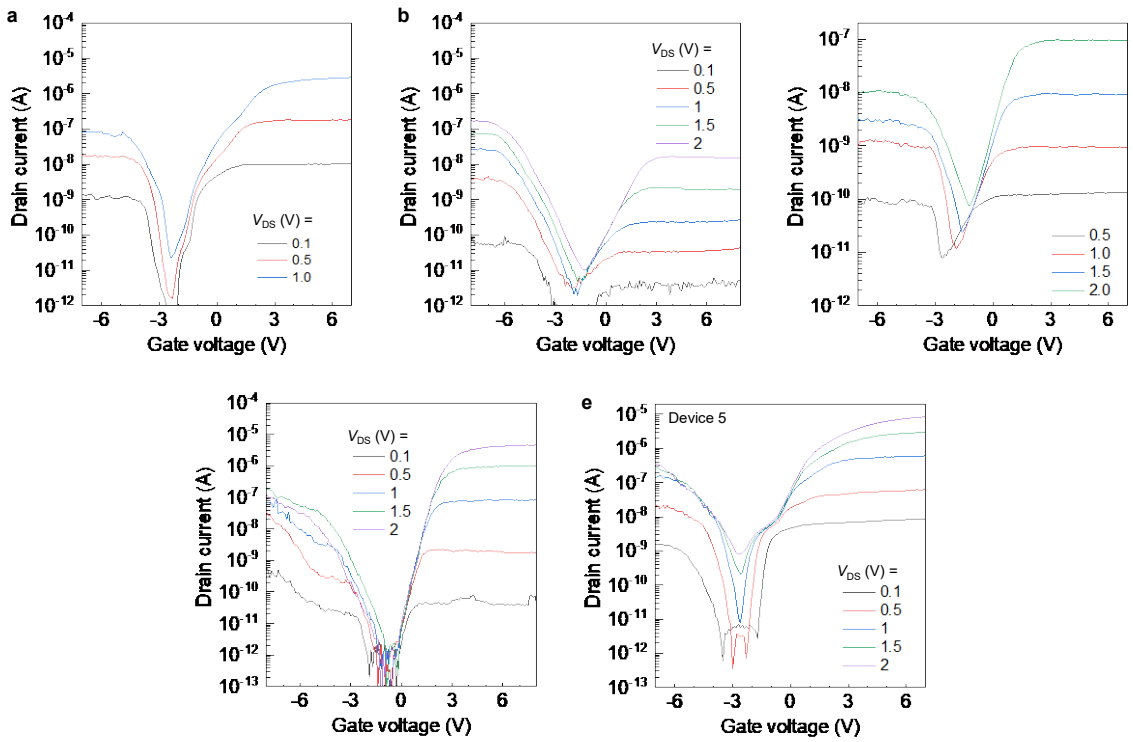

Supplementary Fig. 16. Reproducibility of CBIC–Cu-integrated multilayer WS_2 transistors. a–e, Room temperature transfer curves of top-gated WS_2 transistors fabricated with CBIC–Cu. To confirm reproducibility, we fabricated and measured five additional devices. The devices consistently exhibited ambipolar behaviour with a largely enhanced p-branch, clearly suggesting Fermi level unpinning enabled by the CBIC.

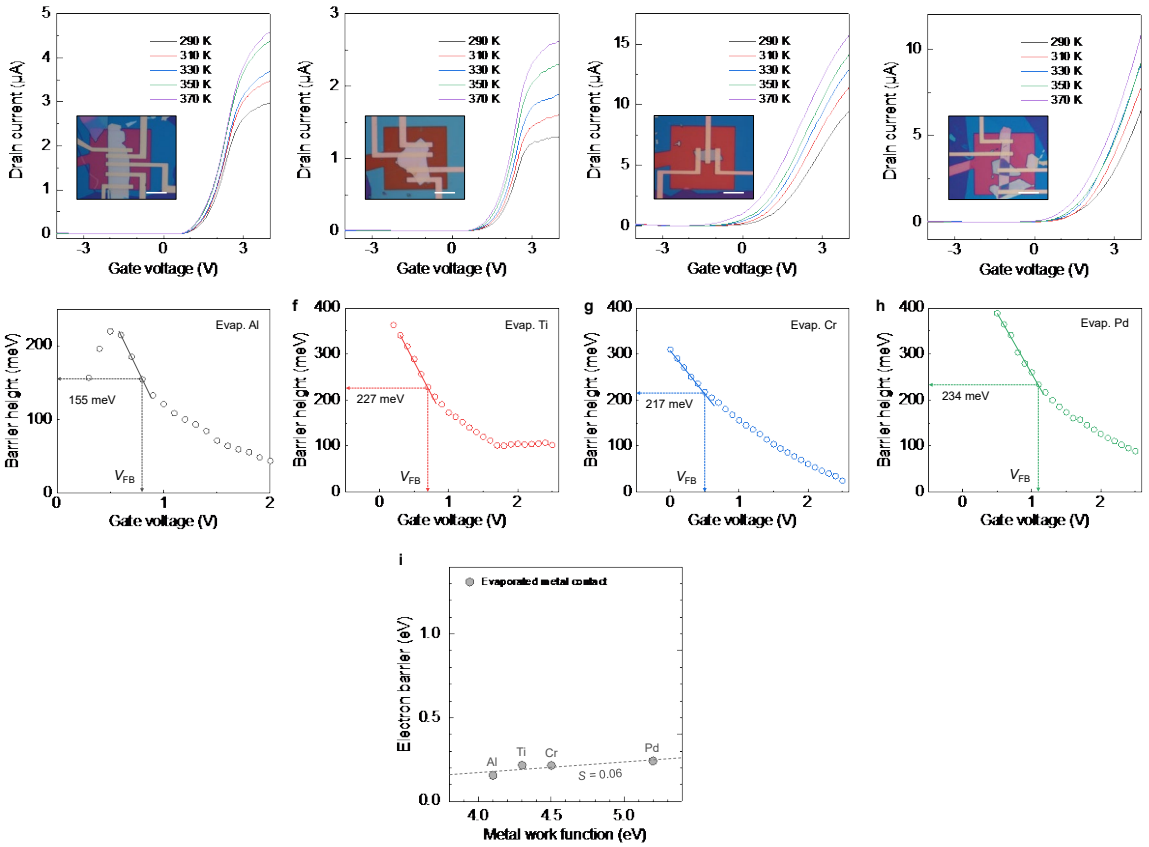

Supplementary Fig. 17. Characterization of contact properties of WS_2 transistors with evaporated metal contacts. a–d, Temperature-dependent transfer characteristics of WS_2 transistors with evaporated Al (**a**), Ti (**b**), Cr (**c**), and Pd (**d**) contacts deposited by electron beam evaporation. Insets are optical microscope images of the corresponding devices. **e–h,** Corresponding effective barrier heights as a function of gate voltage (V_{GS}). The Schottky barrier height was estimated at the flat band gate voltage condition ($V_{GS} = V_{FB}$), which corresponds to the onset of deviation from linear behaviour. **i,** Estimated Schottky barrier heights for different contacts. The series of devices with evaporated metal contacts possessed similar Schottky barrier heights, regardless of their work function, which indicates strong Fermi level pinning at the evaporated metal/WS_2 junctions. The S value of the evaporated metal contacts was estimated from linear fitting, denoted by the grey line. Evap., evaporated.

The Schottky barrier heights of the contacts were extracted using 2D thermionic emission theory, which estimates the activation energy in the thermionic emission region[14,15]. The drain current (I_{DS}) of thermionic emission through a MS junction can be expressed by:

$$I_{DS} = A_{2D}^{*} T^{3/2} \exp\left(-\frac{\phi_B}{k_B T}\right)\left[1 - \exp\left(\frac{-V_{DS}}{k_B T}\right)\right] , \quad (1)$$

where A_{2D}^{*} is the 2D Richardson constant, T is the temperature, k_B is the Boltzmann constant, V_{DS} is the applied drain-to-source voltage, and Φ_B is the effective barrier height at a given gate-source voltage (V_{GS}). When $V_{DS} \gg k_B T$, Eq. (1) can be simplified to:

$$I_{DS} \approx A_{2D}^{*} T^{3/2} \exp\left(-\frac{\Phi_B}{k_B T}\right) . \quad (2)$$

In our device structure (that is, a top-gated transistor with source/drain contacts overlapped with a gate dielectric as shown in Fig. 2d in the main text), Φ_B can be effectively modulated by varying V_{GS}. Using Eq. (2), we can extract Φ_B from the slope of $\ln(I_{DS}/T^{3/2})$ versus $1/T$ plots at various V_{GS} values. The Schottky barrier height (Φ_{SB}) is then estimated at the flat band gate voltage condition ($V_{GS} = V_{FB}$), corresponding to the deviation from the linear dependence of V_{GS} (Fig. S17e–h).

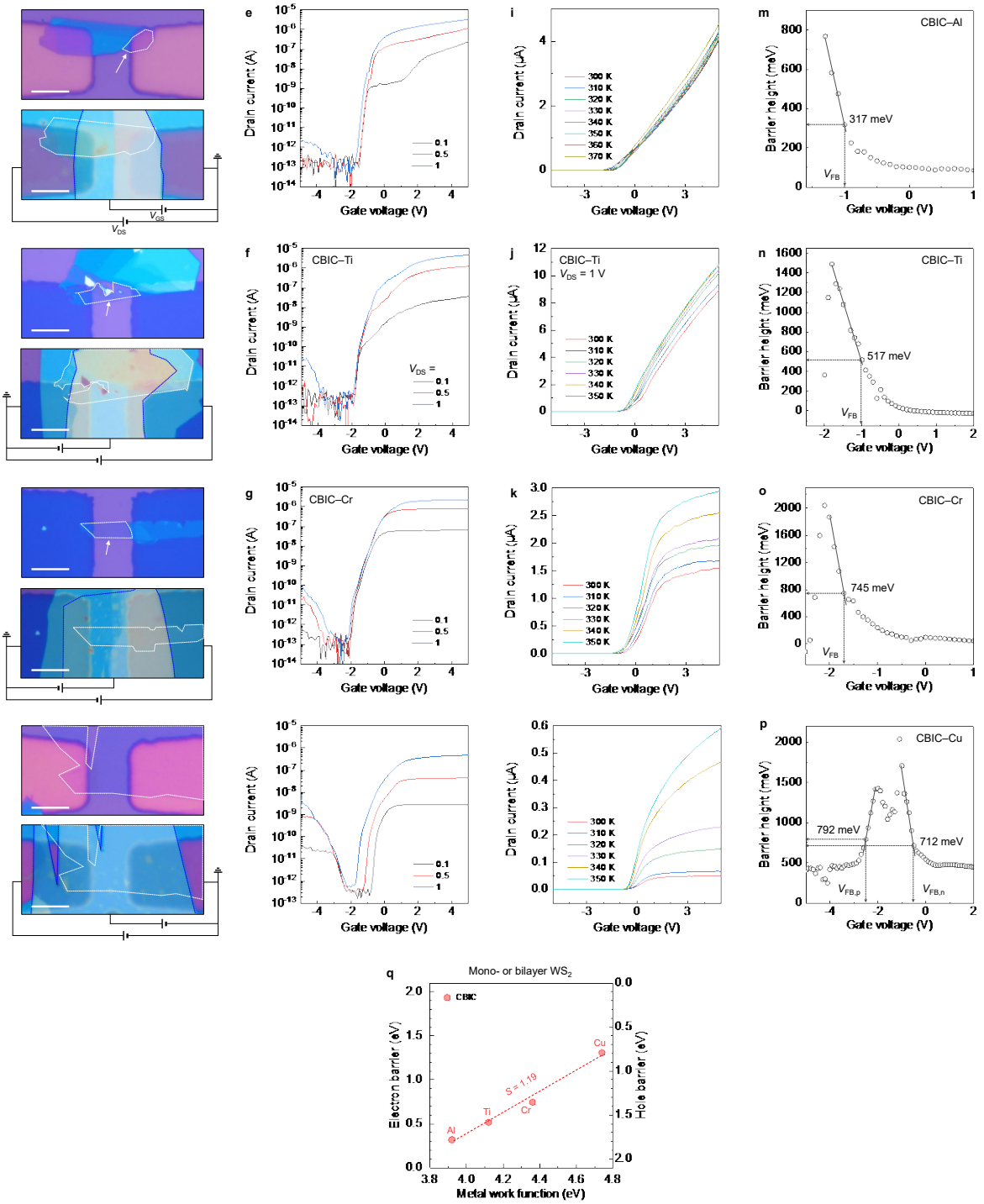

Supplementary Fig. 18. Characterization of the contact properties of ultrathin WS_2 transistors contacted with CBICs. a–d, Optical images of WS_2 flakes (upper) and the corresponding fabricated top-gated WS_2 transistors (lower) integrated with CBIC–Al (**a**), Ti (**b**), Cr (**c**), and Cu (**d**). **e–h,** Room temperature transfer characteristics of the respective devices. **i–l,** Temperature-dependent transfer curves of the respective devices. **m–p,** Effective barrier

heights as a function of gate voltage for the respective devices. **q,** Estimated Schottky barrier heights for different CBICs.

We also validated the Fermi level unpinning effect of the CBIC on ultrathin WS_2 layers. To this end, we fabricated devices using mono- and bilayer WS_2 with various CBICs (Fig. S18a–d), followed by temperature-dependent *I–V* measurements. To rigorously assess the influence of Schottky barrier height, CBIC electrodes in contact with mono- or bilayer WS_2 were used as the source in all electrical measurements. In this configuration, most of the applied drain-to-source voltage (V_{DS}) drops at the reverse-biased contact, suggesting that the FET behaviour is predominantly dictated by the source side. For the CBIC–Al, CBIC–Ti, and CBIC–Cr contacts, the devices exhibited predominantly n-type behaviour (Fig. S18e–g). By contrast, for the CBIC–Cu contact with a much higher work function (4.74 eV), the device exhibited a clear ambipolar characteristic, with the electron current being higher than the hole current (Fig. S18h). These observations are similar to those in the multilayer WS_2 (40–50 nm) transistors with CBICs (Fig. S15).

Our measurements further revealed that for the device with CBIC–Al, the Schottky barrier height for electron injection was 317 meV. With increasing work function of the CBIC, the electron Schottky barrier heights for the CBIC–Ti and CBIC–Cr devices were found to be 517 meV (Fig. S18n) and 745 meV (Fig. S18o), respectively. Finally, for the device with CBIC–Cu, the hole and electron Schottky barrier heights were 792 meV and 712 meV, respectively (Fig. S18p). Figure S18q shows the estimated Schottky barrier height for different CBICs as a function of the corresponding work functions. We note that the overall Schottky barrier height values are slightly higher than those of multilayer WS_2 devices, probably due to the large bandgap of mono- or bilayer WS_2. The Schottky barrier height is highly dependent on the CBIC work functions with a fitted S parameter of 1.19, clearly indicating the Fermi level

unpinning effect. Taken together, these observations verify that the CBIC can form a nearly ideal interface with ultrathin WS_2 layers without pinning.

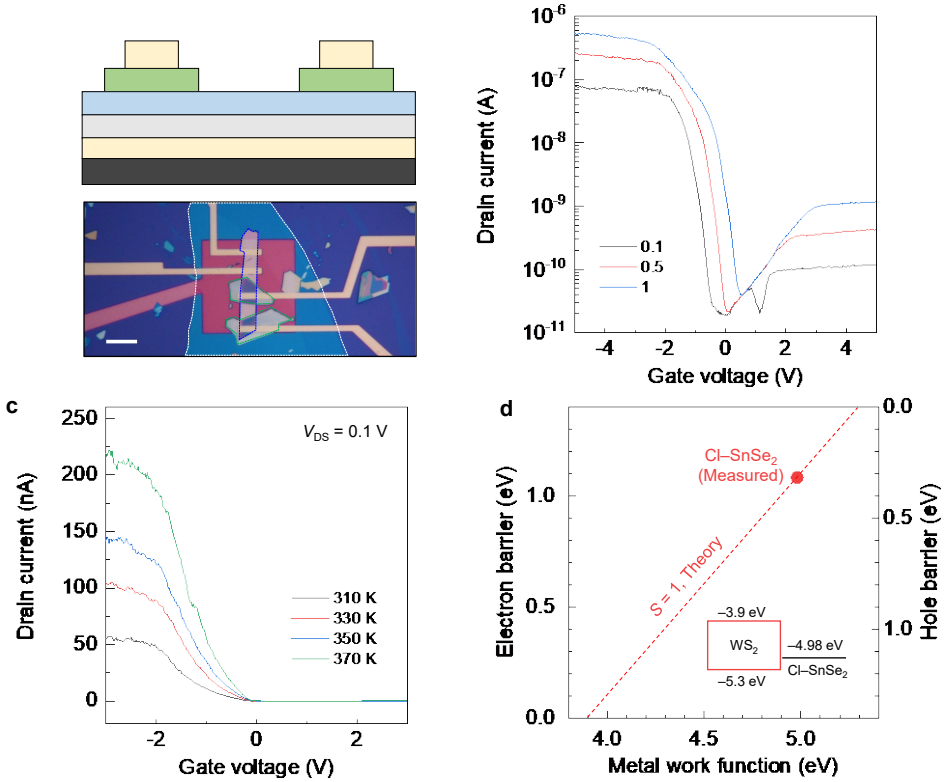

Supplementary Fig. 19. Characterization of the contact properties of Cl–$SnSe_2$-contacted WS_2 transistors. a, Schematic (upper) and optical image (lower) of a bottom-gated WS_2 transistor contacted with Cl–$SnSe_2$. **b,** Room temperature transfer curve of the corresponding device, demonstrating a p-type characteristic due to the high work function of Cl–$SnSe_2$. **c,** Temperature-dependent transfer curves of the same device. **d,** Schottky barrier height of the Cl–$SnSe_2$ contact. The red dashed line indicates the ideal Schottky barrier height calculated from Schottky–Mott theory (S = 1). Inset: Expected band energy level alignment of Cl–$SnSe_2$ metal and multilayer WS_2. As shown in Fig. 2j in the main text, the hole Schottky barrier height of Cl–$SnSe_2$ was measured to be 317 meV (denoted by the red dot in Fig. S19d). This experimental value is in good agreement with the calculated hole Schottky barrier value of 320 meV, indicating a high-quality contact without Fermi level pinning.

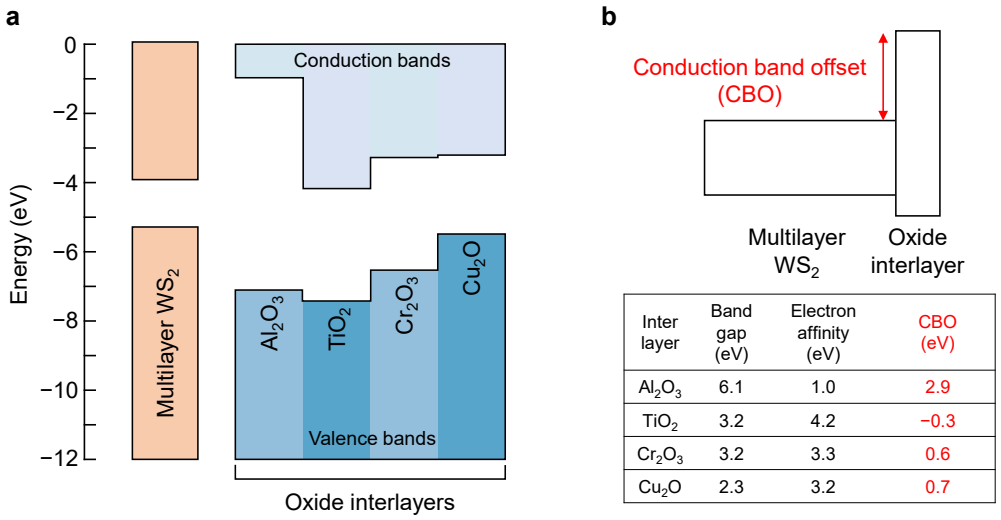

Inter layer	Band gap (eV)	Electron affinity (eV)	CBO (eV)
Al_2O_3	6.1	1.0	2.9
TiO_2	3.2	4.2	−0.3
Cr_2O_3	3.2	3.3	0.6
Cu_2O	2.3	3.2	0.7

Supplementary Fig. 20. Band alignment of multilayer WS_2 and various interlayers. a, Band alignment of multilayer WS_2 and the oxide interlayers used in this study. **b,** Schematic describing the conduction band offset (CBO) and a table showing the calculated values for various oxide interlayers exploited in this work. The material parameters were obtained from previous reports in the literature[16,17].

In general, the oxide interlayer may induce tunnelling resistance because electron tunnelling strongly depends on the barrier height and width[18]. In principle, the tunnelling barrier is determined by the conduction band offset (CBO) between the interlayer and the 2D semiconductor. The low CBO between TiO_2 and WS_2 can create a low barrier height between them, resulting in a low-resistance MIS contact without introducing significant tunnelling resistance[12].

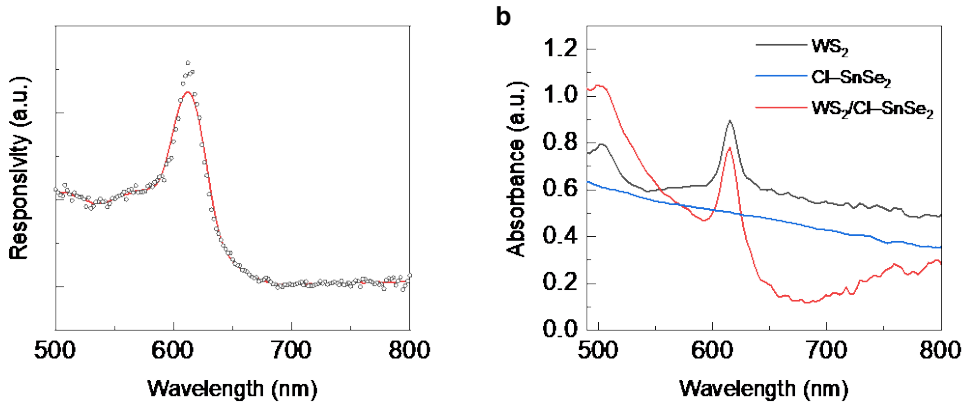

Supplementary Fig. 21. Spectral photoresponsivity of the CBIC device. a, Spectral photoresponsivity of the WS_2 photodetector contacted with CBIC–Al, measured in photovoltaic mode (V = 0 V). The red line is a guide to the eye. **b,** Absorption spectra of the WS_2/Cl–$SnSe_2$ heterostructure.

The spectral responsivity of our photodiode was also investigated. Spectral responsivity measurement was performed using a current preamplifier (SR570, Stanford Research Systems) and a lock-in amplifier (SR830, Stanford Research Systems). The light source used for the measurement was a QTH lamp. The responsivity values were determined by correcting the measured photocurrent with the light intensity of the QTH spectrum[19].

In Fig. S21a, we plot the spectral responsivity of our photodiode consisting of a WS_2/Cl–$SnSe_2$ heterostructure, measured in photovoltaic mode (V = 0 V). Clearly, the photocurrent response of the device follows the absorption spectrum of the WS_2/Cl–$SnSe_2$ heterostructure (Fig. S21b), indicating that photocarrier generation stems from the heterostructure. A responsivity peak is observed at a wavelength around 615 nm, which corresponds to the A-exciton energy level of bulk WS_2[20].

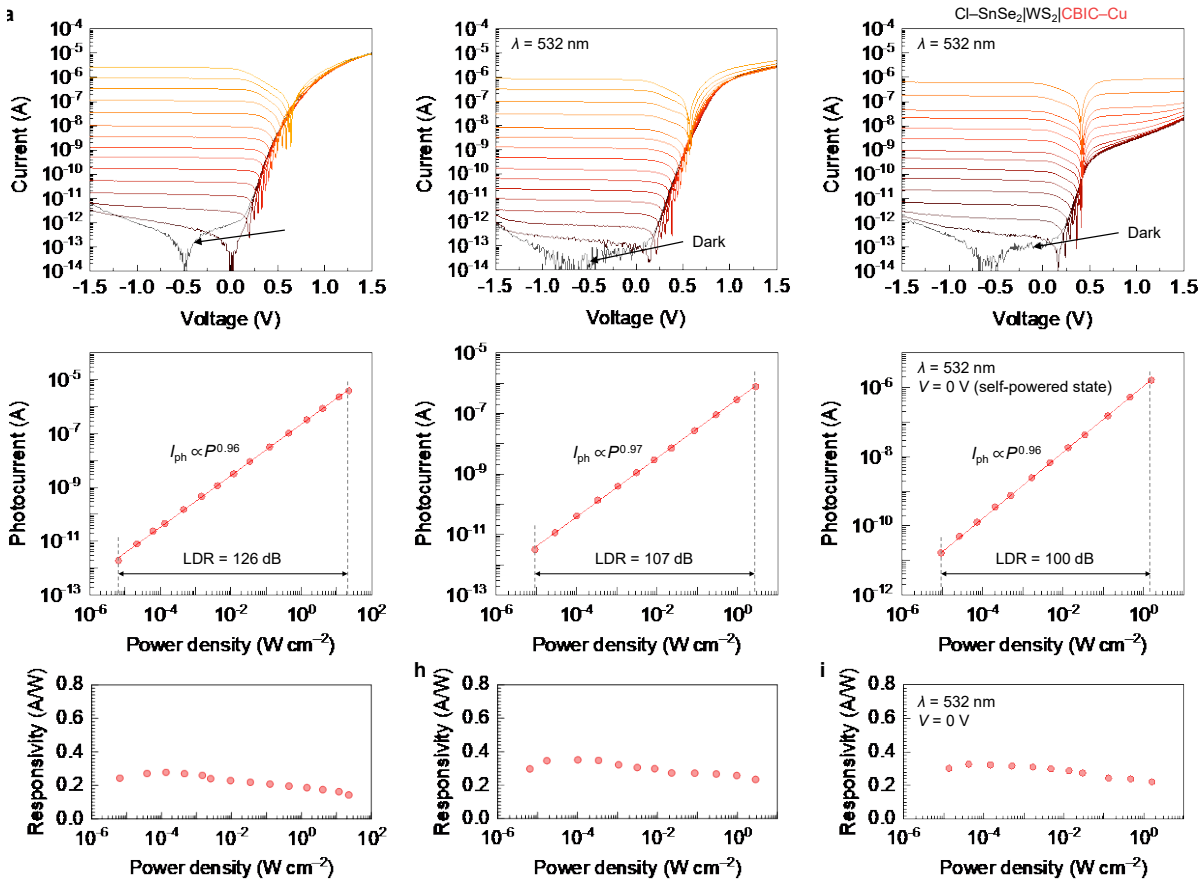

Supplementary Fig. 22. Performance of CBIC-integrated WS_2 photodetectors. a–c, *I–V* characteristics of the WS_2 photodetector integrated with CBIC–Ti (**a**), Cr (**b**), and Cu (**c**) under dark and 532 nm illumination conditions with varying light power densities. **d–f,** Photocurrent of the corresponding devices as a function of light power density, measured at zero bias (self-powered state). The red line shows a power law fit to the experimental data. All devices achieved high linear dynamic range (LDR) values exceeding 100 dB, similar to that of the CBIC–Al-integrated device (shown in the main text). **g–i,** Responsivity of the devices contacted with CBIC–Ti (**g**), Cr (**h**), and Cu (**i**) as a function of optical power density. Our CBIC photodetectors exhibited nearly consistent responsivity values over a wide dynamic range spanning over five orders of magnitude. The slightly higher responsivity observed at very low light intensities may be attributed to trap-limited gain, which results from charge-trapping effects.

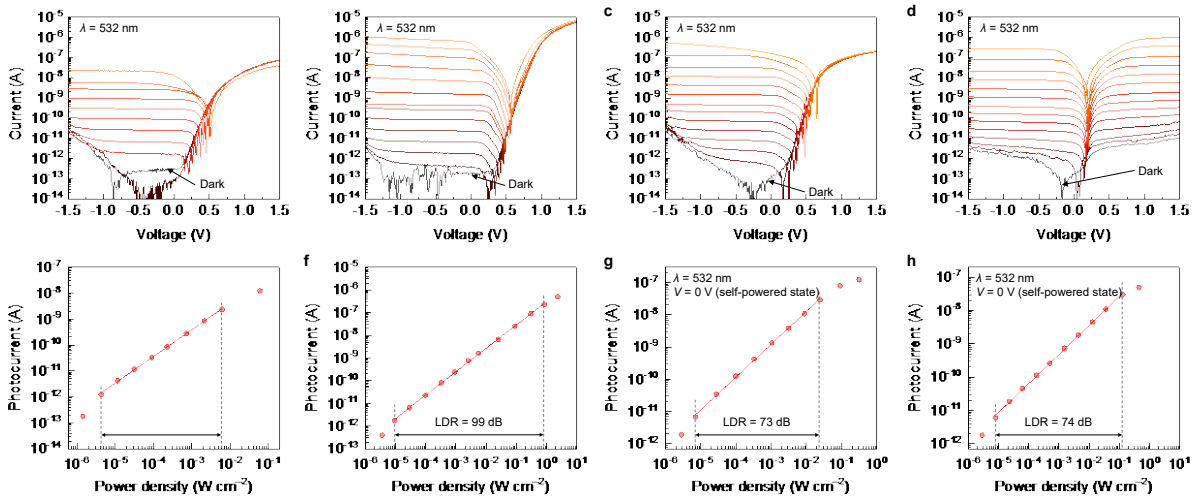

Supplementary Fig. 23. Performance of MIS-contacted WS_2 photodetectors. a–d, *I–V* characteristics of WS_2 photodetectors contacted with MIS–Al (**a**), Ti (**b**), Cr (**c**), and Cu (**d**) under dark and 532 nm illumination conditions with varying light power densities. **e–h,** Photocurrent of the corresponding devices as a function of light power density, measured at zero bias (self-powered state). The red line shows a power law fit to the experimental data. Overall, the MIS devices exhibited inferior performance, with low LDR values of less than 99 dB, when compared with CBIC devices. This can be attributed to high series resistance, primarily caused by the oxide interlayers.

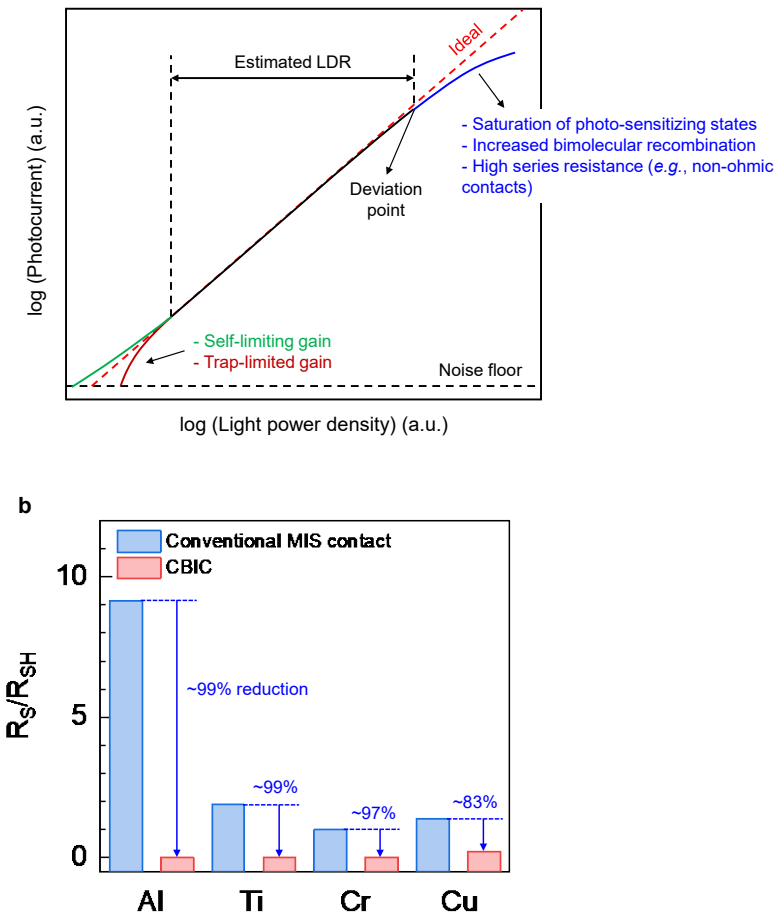

Supplementary Fig. 24. a, Intensity-dependent photocurrent illustrating potential nonlinearity of the responsivity at both low and high light intensities. For low light intensities: self-limiting gain and trap-limited gain. For high light intensities: saturation of photo-sensitizing states, increased bimolecular recombination, and high series resistance. **b,** Comparison of the R_S/R_{SH} ratio of MIS and CBIC devices. R_S and R_{SH} represent series resistance and shunt resistance, respectively, and their values for each device were extracted at an optical power density of ~100 mW cm^{-2}.

The linear dynamic range (LDR), the range over which the responsivity (R) remains constant under different light intensities, is typically limited by several factors, as illustrated in Fig. S24a.

At low light intensities, self-limiting gain leads to superlinear behaviour[21], while trap-limited gain results in sublinear behaviour[22]. These behaviours are usually observed in photodetectors with high photogain and low response speed. Deviation from linearity at high intensities can be attributed to the onset of saturation of photo-sensitizing states, increased bimolecular recombination, or the impact of high series resistance in the device[23].

It is noted that, unlike MIS devices, CBIC devices can maintain a consistent responsivity at intense illumination, which is expected to favour high-dynamic-range sensing (*i.e.*, large LDR). The observed large LDR of the CBIC devices (as compared with MIS devices) can be explained as follows. The Shockley diode equation including series resistance (R_S) and shunt resistance (R_{SH}) can be written as

$$I = I_S\left(e^{\frac{q(V-IR_S)}{nk_BT}} - 1\right) + \frac{V-IR_S}{R_{SH}} \ , \qquad (3)$$

where I_S is saturation current, q is electronic charge, R_S is series resistance, n is an ideality factor, k_B is the Boltzmann constant, T is temperature, and R_{SH} is shunt resistance.

Under light illumination, Eq. (3) can be rewritten as follows:

$$I = I_S\left(e^{\frac{q(V-IR_S)}{nk_BT}} - 1\right) - I_{IL} + \frac{V-IR_S}{R_{SH}} \ , \qquad (4)$$

where I_{IL} is the short-circuit current without parasitic resistance. At the short-circuit condition ($V = 0$ V),

$$I_{PH} = I_S\left(e^{\frac{-I_{PH}R_S}{nk_BT}} - 1\right) - I_{IL} - \frac{I_{PH}R_S}{R_{SH}} \ , \qquad (5)$$

where I_{PH} is the short-circuit photocurrent. Compared to the latter terms of the above equation, the I_S value of the first term shows a much smaller value (typically, < 1 pA for our devices), so this term can be neglected. Thus, Eq. (5) can be simplified to

$$I_{PH} = -\frac{I_{IL}}{\left(1+\frac{R_S}{R_{SH}}\right)} \quad . \qquad (6)$$

From this equation, it is evident that a lower R_S and higher R_{SH} (*i.e.*, a low R_S/R_{SH} value) leads to higher short-circuit photocurrent (I_{PH}) under the same illumination conditions. A shown in Fig. S24b, the CBIC devices typically exhibited relatively low R_S/R_{SH} values under intense illumination (~100 mW cm^{-2}), almost approaching zero. Considering that R_{SH} is highly dependent on the internal electric field (associated with the work function difference between asymmetric heterocontacts), such a substantial reduction in R_S/R_{SH} can be primarily ascribed to the lowering of series resistance (R_S). Therefore, the loss of short-circuit photocurrent due to series resistance (largely due to the insulating nature of the oxide interlayer in conventional MIS contacts) can be significantly minimized, enabling the extension of the photodetection range to high-light-level conditions.

It should also be noted that our CBIC devices feature consistent R and D^* values, particularly under intense illumination, unlike many previous 2D photodetectors that exhibit nonlinearity under such conditions. This consistency can be ascribed to the combined effect of (i) the low R_S of the devices, and (ii) the high R_{SH} due to the presence of a strong internal electric field and highly carrier-selective contacts. In our vertical Schottky diode structure with asymmetric heterocontacts, this leads to a strong internal electric field due to the nanometer-scale thickness of the WS_2 layer (40–50 nm) and a large work function difference between heterocontacts. Consequently, carrier recombination, which acts as a leakage current, is greatly suppressed, resulting in an increased R_{SH}. The loss of short-circuit photocurrent in CBIC devices can

therefore be significantly minimized even under high optical power, facilitating the extension of the photodetection range to high-light-level conditions.

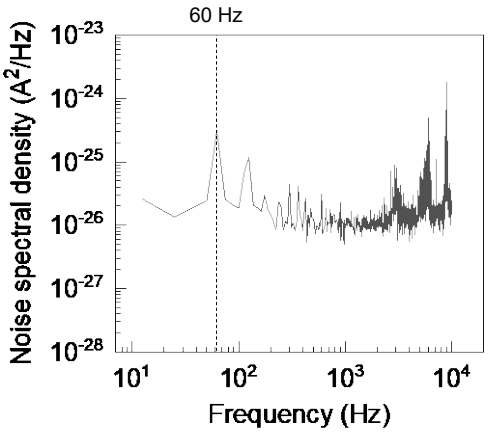

Supplementary Fig. 25. Noise spectral density measurement of the CBIC–Al-integrated WS_2 photodetector. Noise characterization was conducted under a bias of 0 V and room temperature. The highlighted 60 Hz peak is associated with powerline measurement noise.

The specific detectivity (D^*) of the device can be extracted using the following equation:

$$D^* = \frac{R\sqrt{A\Delta f}}{i_n},$$

where R is responsivity, A is the active area of the photodiode, Δf is the electrical bandwidth (1 Hz), and i_n is noise current. Ideally, D^* should be obtained from a precise noise spectral density measurement. To this end, we directly obtained the noise current from noise spectral density measurement over the relevant frequency of our photodetector, as shown in Fig. S25. Overall, the observed shape, which exhibits near frequency-independence, is similar to systems dictated by thermal or Johnson noise, and notably, low-frequency noise ($1/f$) was not observed, indicating that our device primarily operates in photovoltaic mode at zero bias. From this measurement, we extracted a room temperature D^* value of ~2.11×10^{10} cm $Hz^{1/2}$ W^{-1}.

Additionally, when the photodetectors are operated under reverse bias, the shot noise (i_{shot}) may dominate the total noise (i_n). Under this condition, D^* can be expressed as

$$D^* = R\sqrt{\frac{A}{2qI_{\mathrm{d}}}},$$

where A is the active area of the device, q is the unit charge, and I_{d} is the dark current. The calculated D^* of our device could reach up to 3.23×10^{12} cm $\mathrm{Hz}^{1/2}$ W^{-1}. This D^* value is comparable to that of a state-of-the-art 2D photodetector based on a unipolar barrier structure (2.7×10^{12} cm $\mathrm{Hz}^{1/2}$ W^{-1} at 520 nm)[24]. The observed high D^* can be primarily attributed to the ultralow reverse-bias current of our device (on the order of picoamps).

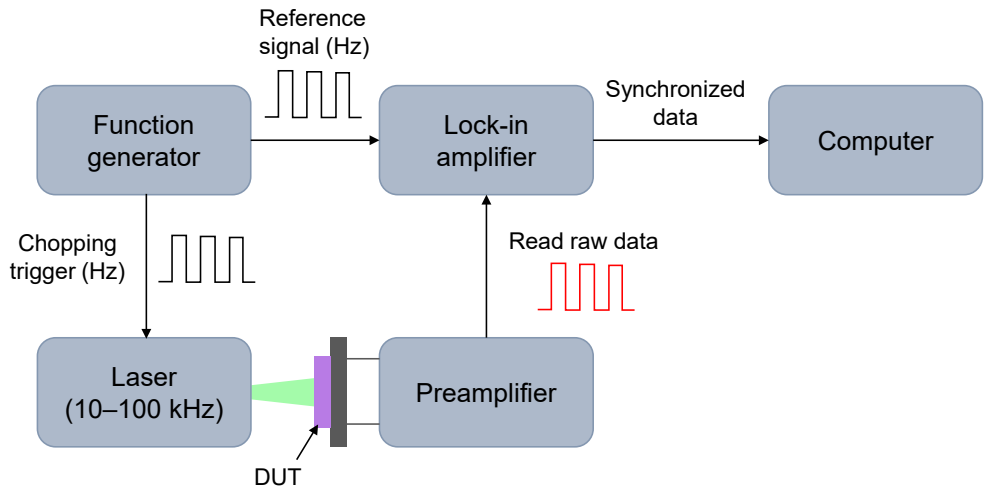

Supplementary Fig. 26. Schematic of the bandwidth measurement system in this study.

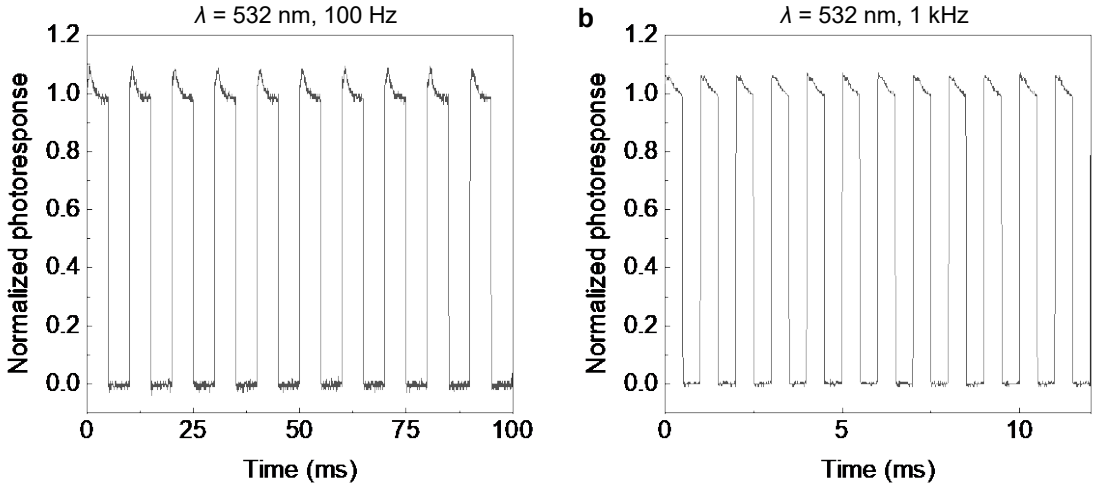

Supplementary Fig. 27. Frequency response of the WS_2 photodetector integrated with CBIC–Al. a,b, Photocurrent measured at zero bias under modulated laser illumination at 100 Hz (**a**) and 1 kHz (**b**).

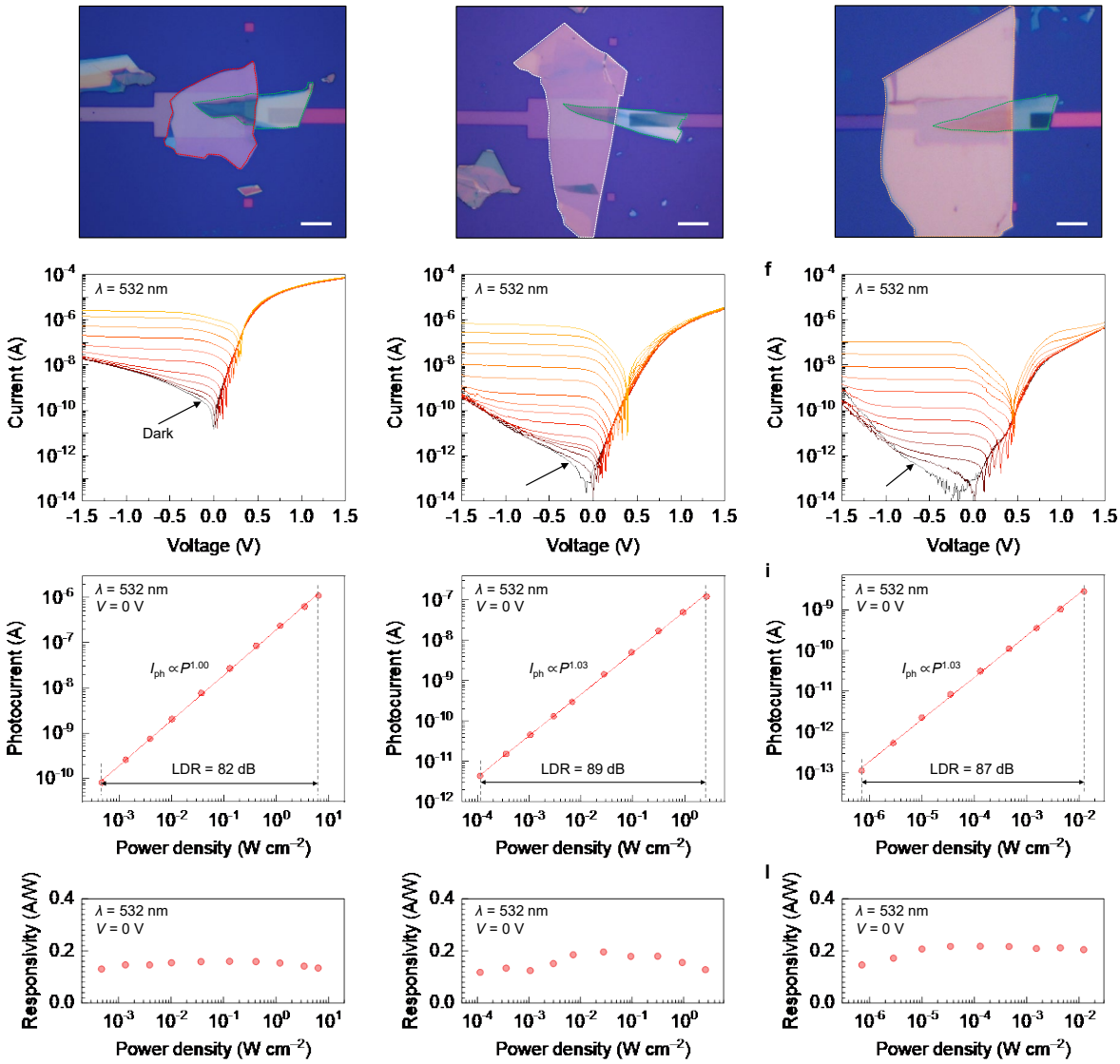

Supplementary Fig. 28. Universality of the CBIC approach. a–c, Optical images of CBIC–Al-integrated MoS_2 (**a**), $ReSe_2$ (**b**), and WSe_2 (**c**) photodetectors. **d–f,** *I–V* characteristics of the MoS_2 (**d**), $ReSe_2$ (**e**), and WSe_2 (**f**) devices under dark and 532 nm illumination conditions with various optical powers. **g–i,** Photocurrent of the devices as a function of light power density, measured at zero bias. The MoS_2 (**g**), $ReSe_2$ (**h**), and WSe_2 (**i**) devices show LDR values of 82, 89, and 87 dB, respectively. The red line shows a power law fit to the experimental data. **j–l,** Responsivity of the devices fabricated with MoS_2 (**j**), $ReSe_2$ (**k**), and WSe_2 (**l**) as a function of optical power density. The results clearly suggest the universality of our CBIC approach.

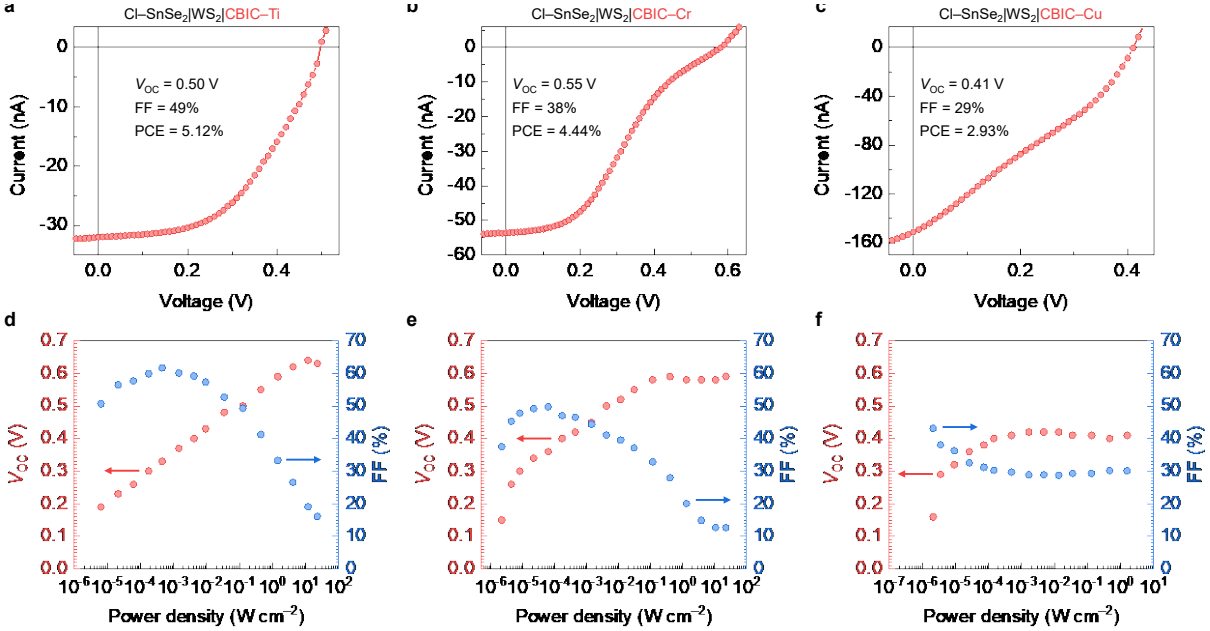

Supplementary Fig. 29. Performance of CBIC-integrated WS_2 photovoltaic cells. a–c, Linear *I–V* characteristics of WS_2 photovoltaic devices with CBIC–Ti (**a**), Cr (**b**), and Cu (**c**) under 532 nm illumination (~100 mW cm^{-2}). PCE, power conversion efficiency. **d–f,** V_{OC} and fill factor (FF) of the corresponding devices as a function of optical power density. We note that both CBIC–Cr and –Cu devices show an s-shaped curve with a high series resistance. This s-shaped behaviour could be caused by a significant energy barrier for charge extraction[1].

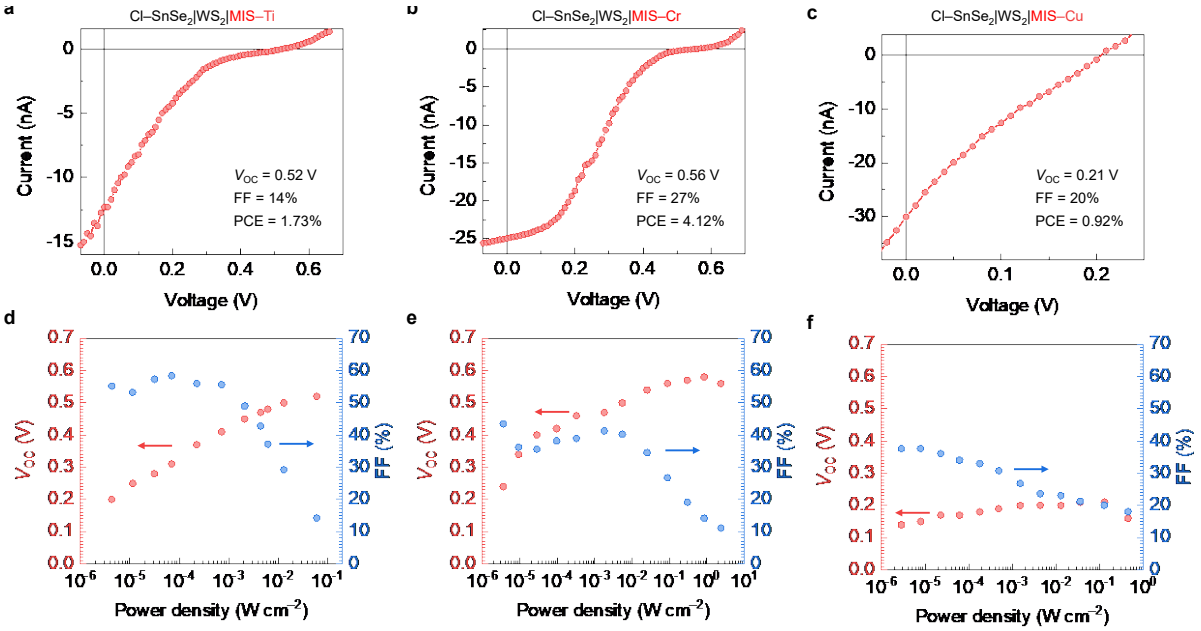

Supplementary Fig. 30. Performance of MIS-contacted WS_2 photovoltaic cells. a–c, Linear *I–V* characteristics of WS_2 photovoltaic device with MIS–Ti (**a**), Cr (**b**), and Cu (**c**) under 532 nm illumination (~100 mW cm^{-2}). **d–f,** V_{OC} and FF of the corresponding devices as a function of optical power density. We note that all MIS devices show a pronounced s-shaped curve. Such s-shaped behaviour is largely attributed to high series resistance resulting from oxide interlayers, as previously reported[1].

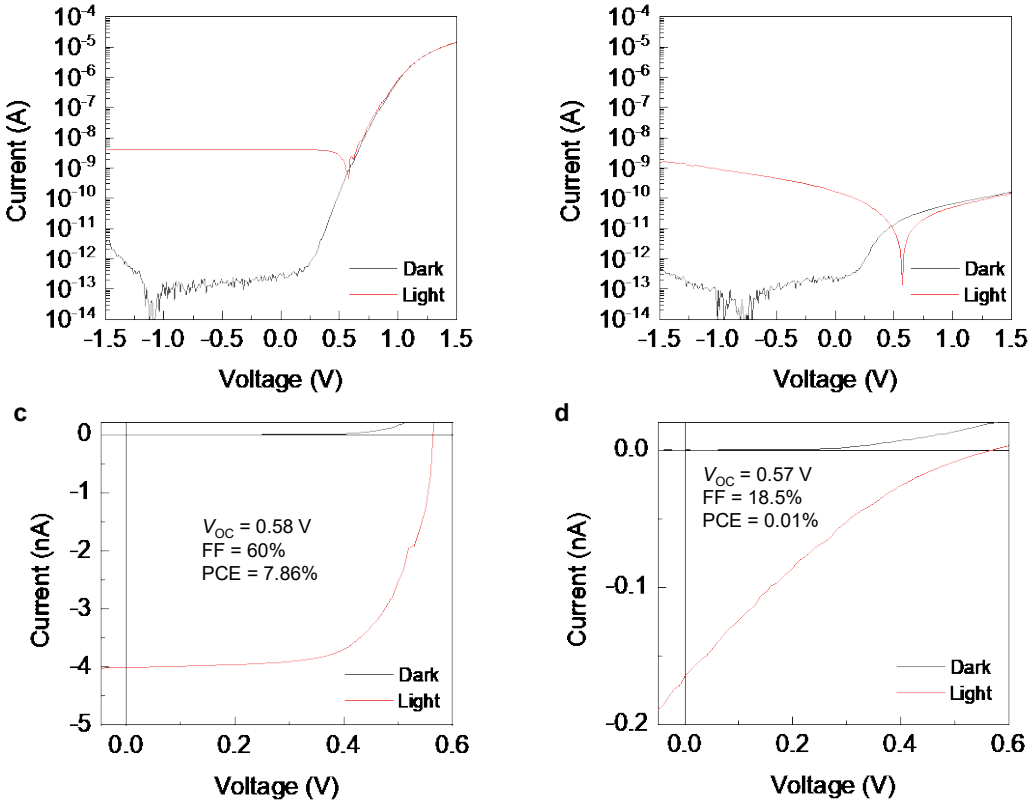

Supplementary Fig. 31. **Device stability of the CBIC–Al contact. a,b,** *I–V* curves for initial (**a**) and after one month ambient exposure (**b**) of a WS_2 device contacted with CBIC–Al. **c,d,** Linear plots of the same data in **a,b**.

CBICs with a low work function can offer benefits such as efficient transport of electrons in and out of devices, potentially maximizing the power conversion efficiency of various photovoltaic devices. However, there are underlying trade-offs associated with using low work function metals, such as Al, in CBICs. Particular attention must be given to their reactive chemical nature and device reliability; low work function metals are often very chemically reactive, which could lead to progressive oxidation of the interlayer over time (*e.g.,* for Al metal, a thicker and denser AlO_x layer), consequently affecting the long-term reliability of CBIC-based photovoltaic devices due to increased series resistance of contacts (Fig. S31). To prevent oxidation, subsequent surface passivation and/or encapsulation of the whole device are

potential paths. Despite the environmental instability, the unique characteristics presented by the CBIC architecture—Fermi level unpinning, work function tunability, ease of fabrication, and low series resistance compared to conventional MIS contact structures—suggest considerable potential for both fundamental studies and applied technologies in the fields of 2D materials and various photovoltaics applications.

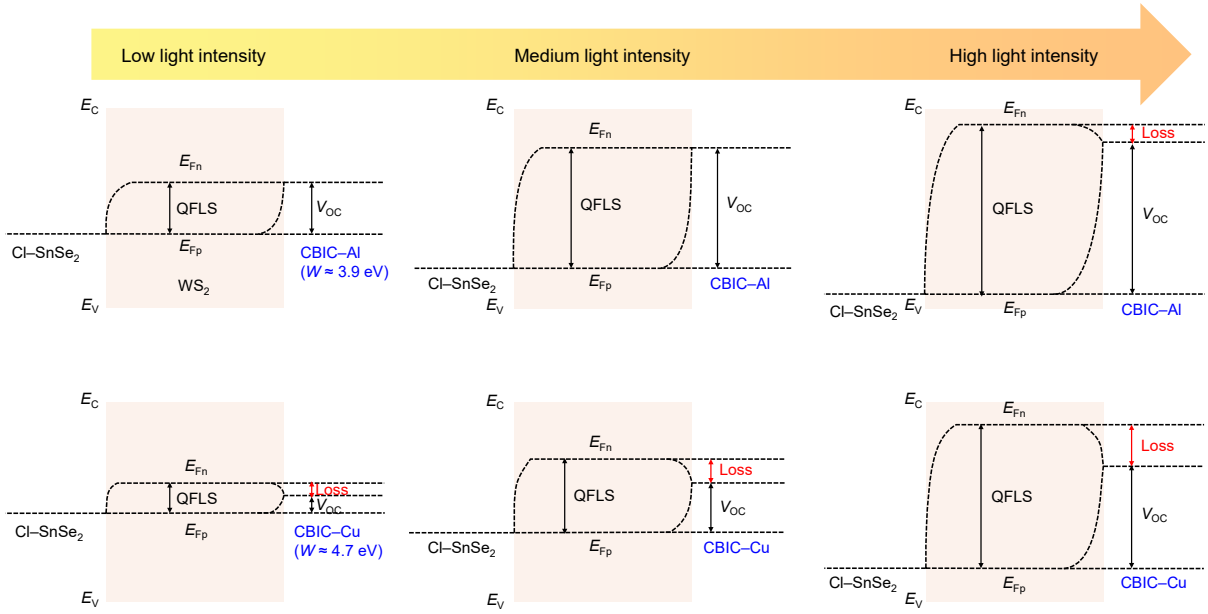

Supplementary Fig. 32. Schematic band diagram illustrating the open-circuit voltage (V_{OC}) for various light intensities in WS_2 photovoltaic cells fabricated with CBIC–Al and –Cu. The schemes are based on the results of drift-diffusion simulations conducted with SCAPS. The diagrams highlight the detrimental effects of using high work function electrodes, particularly under high light illumination. E_{Fn} and E_{Fp} represent the quasi-Fermi levels for electrons and holes, respectively. QFLS, quasi-Fermi-level splitting; E_C, conduction band minimum; E_V, valence band maximum.

Figure S32 shows band diagrams depicting the relation between quasi-Fermi-level splitting (QFLS) and V_{OC} for various light intensities in WS_2 devices with different CBIC electrodes. The schemes show that the quasi-Fermi levels (E_{Fn} and E_{Fp}) remain almost constant within the WS_2 bulk, while band bending occurs at the WS_2/CBIC interfaces. As a result, there is a significant decrease in V_{OC} (referred to as 'V_{OC} loss'), leading to a mismatch with the QFLS in the bulk. More importantly, this V_{OC} loss becomes more pronounced when using high work

function electrodes and when under high irradiation, which is of particular importance for the realization of practical 2D photovoltaics.

Additionally, the schemes in Fig. S32 also emphasize that V_{OC} does not necessarily represent the recombination mechanisms occurring in the bulk of the absorber layer. In 2D photovoltaic cells, V_{OC} can be constrained by the work function difference between the heterocontacts, particularly when this difference is smaller than the quasi-Fermi level difference created by the absorber layer. This understanding can be utilized for future 2D photovoltaic devices and contact design optimization. As supported by the current results, to fully exploit the potential of 2D materials, it is crucial to minimize the V_{OC} losses due to contact recombination, especially under operational conditions with high light intensity.

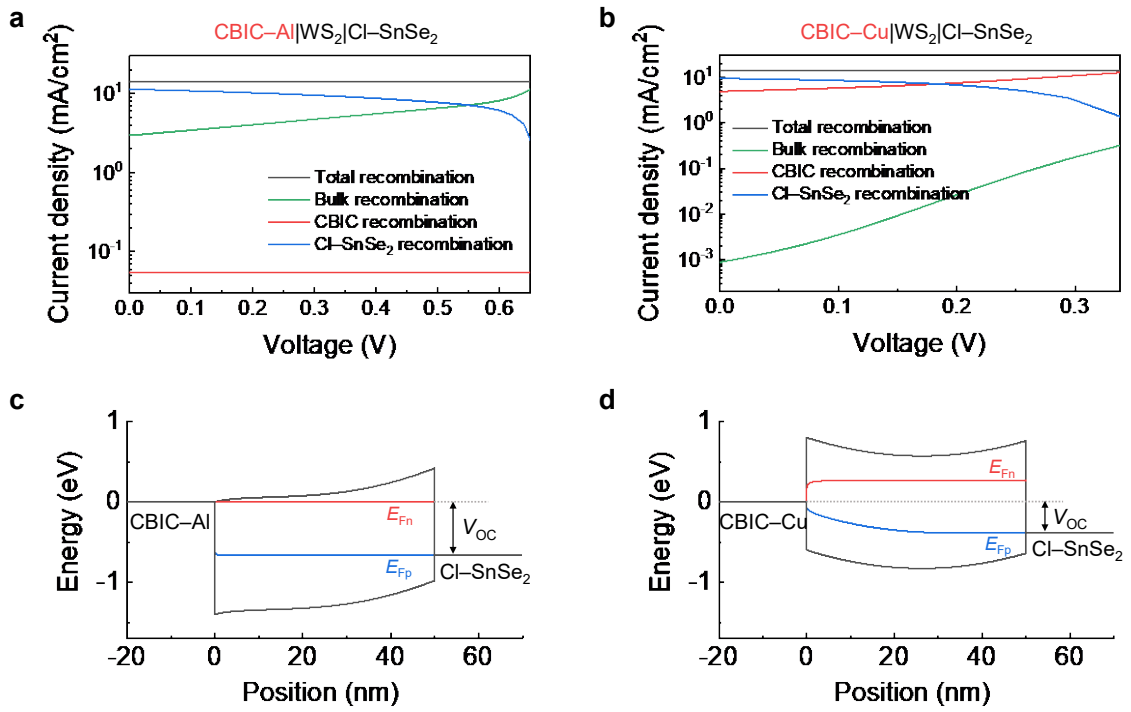

Supplementary Fig. 33. Simulated recombination currents of WS_2 photovoltaic cells with different CBIC electrodes. a,b, Simulation results for the recombination current in WS_2 devices contacted with CBIC–Al (**a**) and CBIC–Cu (**b**). For CBIC–Cu with a higher work function, significant recombination at contacts occurs (indicated by the red line) and consequently dominates the total recombination. **c,d,** Corresponding simulated energy band diagrams for the devices with CBIC–Al (**c**) and CBIC–Cu (**d**) at open-circuit voltage (V_{OC}). All simulations were performed under light illumination conditions (532 nm, 100 mW cm^{-2}). E_{Fn} and E_{Fp} represent the quasi-Fermi levels for electrons and holes, respectively.

Drift-diffusion simulation allows to identify the recombination processes in the devices. Supplementary Fig. 33a,b show the portions of the different recombination mechanisms for devices with a low work function (CBIC–Al) and high work function (CBIC–Cu) electrode, respectively. For the CBIC–Al device with a low work function, negligible recombination at CBIC–Al can be observed. In contrast, for the CBIC–Cu device with a higher work function,

the contribution of recombination at the CBIC–Cu interface (indicated by the red line) becomes significant and cannot be neglected. Such a large contact recombination is also reflected in the downward bending of E_{Fn} near the CBIC–Cu interface in the simulated band diagram under light illumination (Fig. S33d). Given that we used identical simulation parameters except for the work function of the CBIC, the different behaviours are a consequence of the Schottky barrier at the contacts. In principle, ideal photovoltaic devices would feature a zero barrier height with no charge carrier recombination at the contacts. However, in practice, the presence of a nonzero contact barrier can impede charge extraction and, consequently, lead to severe contact recombination; charge carriers become unextractable due to the high energy barrier, and might recombine with minority carriers at the contacts.

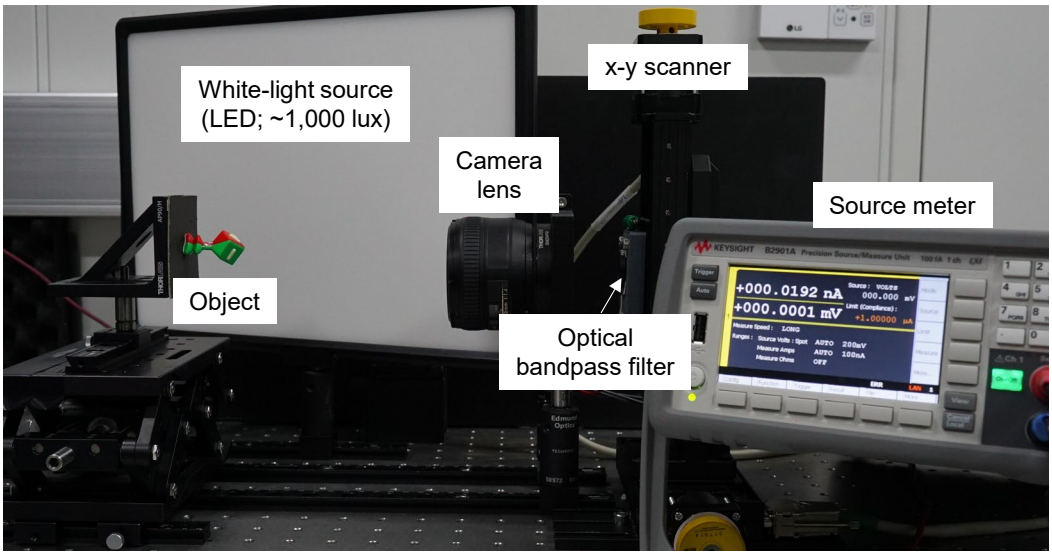

Supplementary Fig. 34. Photograph of the experimental set-up for 3D (or 2D) imaging.

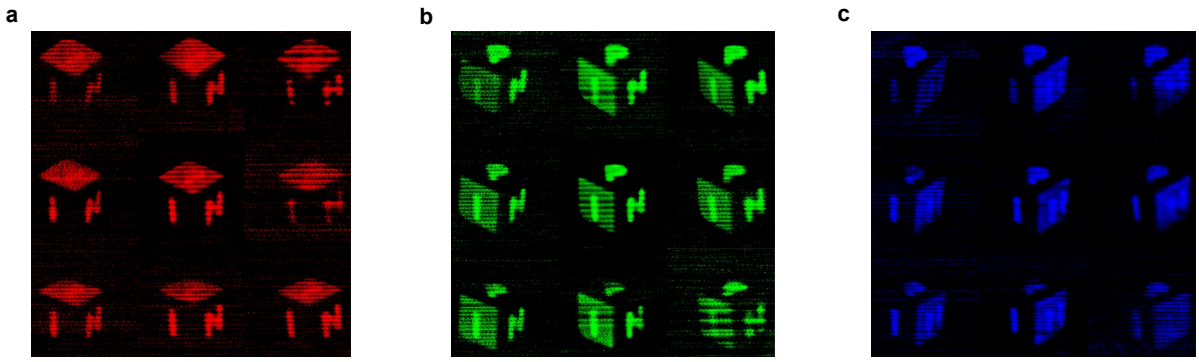

Supplementary Fig. 35. Acquisition of RGB elemental images. a–c, 3 × 3 elemental images acquired at various wavelengths: (**a**) red (650 nm), (**b**) green (550 nm), and (**c**) blue (450 nm).

By adjusting the object's position and considering the lens position, sub-images of the elemental images can depict the 3D object from various perspectives. In this procedure, the object's position was adjusted by displacing it 20 mm horizontally and vertically from the center of the 3 × 3 array. The scanning process was conducted a total of 27 times, with 9 iterations for each wavelength (red, green, and blue). Each scanning cycle took approximately 12 h. Scanning times can be reduced by fabricating large-scale photodiode arrays with a higher device density. In obtaining the final full-colour image, all RGB photocurrent processing was conducted with minimal filtering in MATLAB.

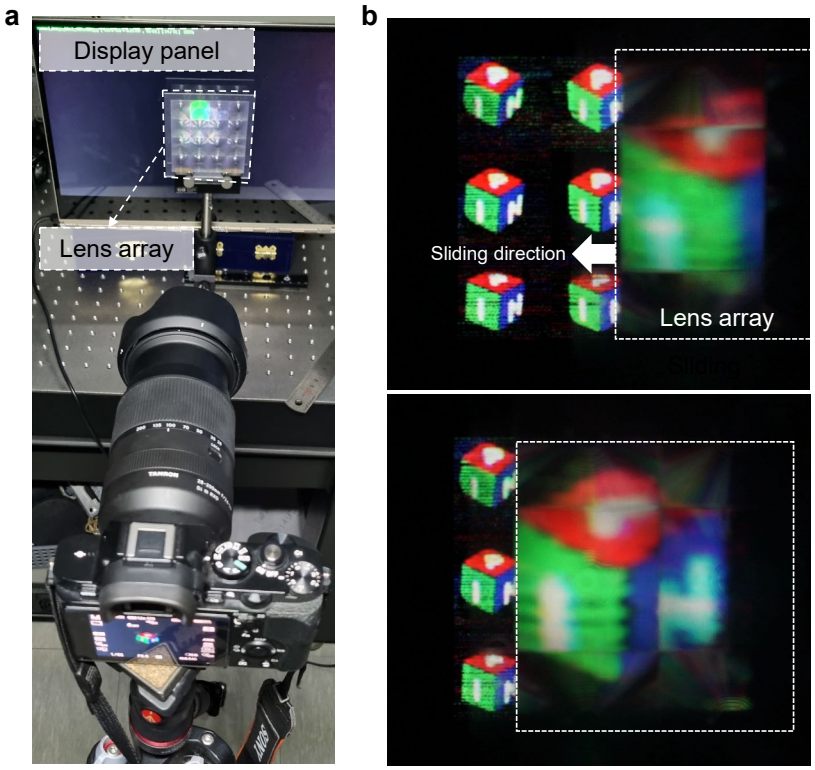

Supplementary Fig. 36. Reconstruction process for 3D integral imaging. a, Photograph of reconstruction system. **b,** Process flow of 3D reconstruction using lens array. The lens array used in this process has a focal length of 22 mm and a sub-lens size of 19 mm. A display panel (3840(H) × 2160(V), 13.9" display, PPI 317) was employed. By integrating partial elements from each sub-lens image, we achieved a realistic depiction of the 3D object from diverse perspectives (see Supplementary Video 1 for more details).

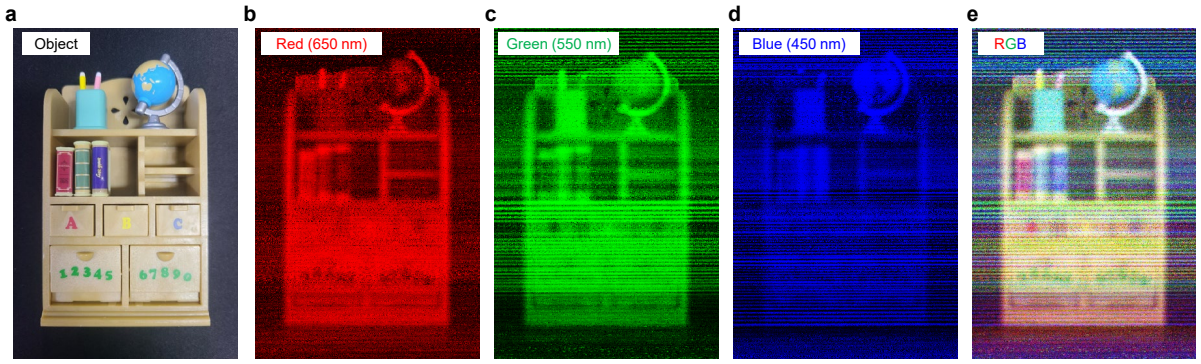

Supplementary Fig. 37. Demonstration of 2D imaging using the CBIC–AI device. a, Photograph of the object. **b–e,** 2D images acquired at various wavelengths: (**b**) red (650 nm), (**c**) green (550 nm), and (**d**) blue (450 nm). **e,** A full-colour 2D image. For 2D imaging, we used the identical experimental set-up as in Supplementary Fig. 35 except for the target object. The size of the object used in the imaging is 58 mm in width and 100 mm in height. Despite the use of the reflective imaging system and the complexity of the object, the resulting image captured by our CBIC-based imager effectively depicts the target object.

Supplementary Table 1. Performance of state-of-the-art 2D photodetectors

Device	Wavelength	Bias (V)	Responsivity (A W^{-1})	Detectivity (cm $Hz^{1/2}$ W^{-1})	Response speed	Linear dynamic range (dB)	Application	Reference
WSe_2/MoS_2 (p–n diode)	532 nm	0	0.17	—	< 0.1 ms	123	—	[25]
InSe (Schottky diode)	400 nm	0	0.35	1.26×10^{13}	200 ns	~40	—	[26]
$WSe_2/ReSe_2$ (p–n diode)	638 nm	0	0.48	6×10^{8}	2 μs/2.5 μs	108	Digital incoherent holographic 3D imaging	[27]
WSe_2 (phototransistor)	532 nm	1	0.18	3.37×10^{11}	13 ms	70.6	—	[19]
WSe_2 (phototransistor)	500 nm	1	0.17	1.2×10^{11}	8 ns	112	—	[28]
$GeSe/MoTe_2$ (p–n diode)	808 nm	0	0.0514	4.14×10^{11}	26 ms	118	—	[29]
MoS_2 (Schottky diode)	638 nm	0	0.07	—	8 μs /6.5 μs	106	3D imaging (transmissive type)	[30]
WS_2/*h*-BN/$PdSe_2$ (unipolar barrier structure)	520 nm	−0.5	—	2.7×10^{12}	74 μs /26 μs	—	—	[24]
BP /MoS_2/Graphene (unipolar barrier structure)	3.8 μm	—	—	2.3×10^{10}	28 μs /23 μs	—	Infrared 2D imaging	[24]
CBIC–Al/WS_2/Cl–$SnSe_2$	**532 nm**	**0**	**0.29**	**2.11×10^{10}**	**4.21 μs /3.95 μs**	**122**	**Full-colour, 3D imaging (reflective type)**	**This work**

Supplementary Table 2. Photovoltaic performance of 2D TMDCs-based p–n and Schottky photodiodes

Device	Illumination	J_{SC} (mA cm^{-2})	V_{OC} (V)	FF (%)	PCE (%)	Reference
p–n junction photodiodes						
MoO_x-WS_2/WS_2 (lateral)	AM 1.5G (100 mW cm^{-2})	4.78	0.6	54	1.55	[31]
n-MoS_2/p-MoS_2 (vertical)	AM 1.5G (100 mW cm^{-2})	3	0.6	22	0.4	[32]
$MoSe_2$/WSe_2 (lateral)	514 nm laser (619 mW cm^{-2})	—	0.06	—	0.12	[33]
WSe_2/MoS_2 (lateral)	White light (1 mW cm^{-2})	0.02	0.22	39	0.2	[34]
WSe_2/MoS_2 (lateral)	AM 1.5G (100 mW cm^{-2})	—	0.39	37.01	2.56	[35]
WS_2/WSe_2 (lateral)	514 nm (30 nW)	—	0.47	—	0.9	[36]
mono-WSe_2/MoS_2 (vertical)	White light (640 mW cm^{-2})	0.58	0.56	50	0.2	[37]
Graphene/WSe_2/MoS_2/Au (vertical)	633 nm laser (7.4×10^5 mW cm^{-2})	1111.1	0.35	45	3.4	[38]
WSe_2/MoS_2 (decorated with PbS QDs) (vertical)	785 nm laser (1.4×10^5 mW cm^{-2})	149.16	0.42	43	7.65	[39]
MoS_2/AsP (lateral)	520 nm laser (10,800 mW cm^{-2})	—	0.61	50	9	[40]
Schottky junction photodiodes						
Ag/WS_2/Au	AM 1.5G (100 mW cm^{-2})	4.1	0.256	44	0.46	[41]
ITO/WS_2/Au	AM 1.5G (100 mW cm^{-2})	5.5	0.57	—	1.7	[42]
Pt/WSe_2/Au	AM 1.5G (100 mW cm^{-2})	10.7	0.38	44	1.6	[43]
Graphene/WO_x/WSe_2/Pt	AM 1.5G (100 mW cm^{-2})	19.61	0.47	59	5.44	[44]
MoO_x/Graphene/WSe_2/Au	AM 1.5G (100 mW cm^{-2})	17.3	0.476	61.7	5.1	[45]
Graphene/WS_2/Pt	AM 1.5G (100 mW cm^{-2})	—	0.4	39	5	[46]
	365 nm laser (57 mW cm^{-2})	—	0.4	43	6.2	
	532 nm laser (54 mW cm^{-2})	—	0.4	42	6.3	

CBIC–Al/WS_2/Cl–$SnSe_2$	**532 nm laser (44 mW cm^{-2})**	**12.23**	**0.66**	**54**	**9.91**	**This work**
	532 nm laser (167 mW cm^{-2})	**45.98**	**0.7**	**51**	**9.83**	

Supplementary Table 3. Multilayer WS_2 parameters for SCAPS-1D simulation

Parameter	Value	Source
Thickness (nm)	50	
Bandgap (eV)	1.4	Ref. 47
Electron affinity (eV)	3.92	Ref. 48
Dielectric permittivity (relative)	13.6	Ref. 41
Conduction band effective density of states (cm^{-3})	4.75×10^{18}	Ref. 49
Valence band effective density of states (cm^{-3})	7.37×10^{18}	Ref. 49
Out-of-plane mobility (for electrons and holes) (cm^2/Vs)	0.01	Ref. 41
Shallow uniform donor density, N_D (cm^{-3})	3.4×10^{17}	Ref. 46
Defect type	Donor	Ref. 41
Energetic distribution	Single	Ref. 41
Total defect density (cm^{-3})	1×10^{14}	Ref. 41

WS_2 thickness: Thicknesses of the WS_2 layer were chosen to reflect our device architecture.

Bandgap: The bandgap of multilayer WS_2 was taken from ref. 47.

Electron affinity: The electron affinity of multilayer WS_2 was taken from ref. 48.

Dielectric permittivity: The dielectric permittivity of multilayer WS_2 was taken from ref. 41.

Conduction (valence) band effective density of states: The effective densities of states for the conduction and valence bands (N_C and N_V, respectively) were calculated using the following equations:

$$N_C = 2\left(\frac{m_e^* k_B T}{2\pi\hbar^2}\right)^{\frac{3}{2}}$$

$$N_{\mathrm{V}} = 2\left(\frac{m_{\mathrm{h}}^{*} k_{\mathrm{B}} T}{2\pi\hbar^{2}}\right)^{\frac{3}{2}}$$

where k_{B} is the Boltzmann constant, T is the temperature, and $\hbar$ is the reduced Planck constant. The effective masses of electrons and holes (m_{e}^{*} and m_{h}^{*}, respectively) were taken from ref. 41.

Electron (hole) mobility: Out-of-plane mobilities were chosen to reflect the vertical charge transport of our device structure. Out-of-plane mobilities of multilayer WS_2 for both electron and hole were taken from ref. 41.

Donor density: WS_2 is known as a lightly n-type material, and its electron concentration was taken from ref. 46.

Total defect density: Parameters related to defects were selected using SCAPS standard settings to reflect our realistic samples.

Work function of electrodes: Work functions of CBIC–Al and –Cu were taken from our KPFM results (Fig. 2b in the main text).

Supplementary Table 4. Specifications of the 3D integral imaging system

Component	Specification	
Lens array	Number of elemental lenses	3 × 3
	Sub-lens size	19 mm
	Focal length	22 mm
x-y stage	Range	11 mm
	Step size	55 μm
Bandpass filter	Wavelength	650 nm (red)
		550 nm (green)
		450 nm (blue)
Display	Pixel size	80 μm
	Resolution (H × V)	3840 × 2160
Object	Size	15 mm × 15 mm
Light source	Intensity	~1,000 lux
Distance (reconstruction process)	Display panel to lens array	15 mm
	Lens array to camera	300 mm

References

1. Seo, J. H. et al. High efficiency inorganic/organic hybrid tandem solar cells. *Adv. Mater.* **24**, 4523–4527 (2012).
2. Jang, J. et al. Fermi-level pinning-free WSe_2 transistors via 2D van der Waals metal contacts and their circuits. *Adv. Mater.* **34**, 2109899 (2022).
3. Murali, K., Dandu, M., Watanabe, K., Taniguchi, T. & Majumdar, K. Accurate extraction of Schottky barrier height and universality of Fermi level de-pinning of van der Waals contacts. *Adv. Funct. Mater*. **31**, 2010513 (2021).
4. Xu, L. et al. An electronic phase diagram of hole-doped BiCuSeO crystals determined by transport characterization under various growth conditions. *CrystEngComm* **23**, 273–281 (2021).
5. Sritharan, T., Li, Y. B., Xu, C. & Zhang, S. Oxidation of Al-Au intermetallics and its consequences studied by x-ray photoelectron spectroscopy. *J. Mater. Res.* **23**, 1371–1382 (2008).
6. Piao, H., Fuller, M. S., Miller, D. & McIntyre, N.S. A study of thin film Au–Al alloy oxidation in ambient air by X-ray photoelectron spectroscopy (XPS), X-ray absorption near edge structure (XANES), and secondary ion mass spectrometry (SIMS). *Appl. Surf. Sci.* **187**, 266–274 (2002).
7. Fuggle, J. C., Källne, E., Watson, L. M. & Fabian, D. J. Electronic structure of aluminum and aluminum-noble-metal alloys studied by sof-X-ray and X-ray photoelectron spectroscopies. *Phys. Rev. B* **16**, 750–761 (1977).
8. Boyen, H. G. et al. Oxidation-resistant gold-55 clusters. *Science* **297**, 1533–1536 (2002).
9. Giannozzi, P. et al. QUANTUM ESPRESSO: a modular and open-source software project for quantum simulations of materials. *J. Phys. Condens. Matter* **21**, 395502 (2009).
10. Perdew, J. P., Burke, K. & Ernzerhof, M. Generalized gradient approximation made simple. *Phys. Rev. Lett.* **77**, 3865–3868 (1996).
11. Chen, P. et al. Multifunctional ytterbium oxide buffer for perovskite solar cells. *Nature* **625**, 516–522 (2024).
12. Jang, J. et al. Clean interface contact using a ZnO interlayer for low-contact-resistance MoS_2 transistors. *ACS Appl. Mater. Interfaces* **12**, 5031–5039 (2020).
13. Liu, Y. et al. Approaching the Schottky-Mott limit in van der Waals metal-semiconductor junctions. *Nature* **557**, 696–700 (2018).
14. Wang, Y. et al. P-type electrical contacts for 2D transition-metal dichalcogenides. *Nature* **610**, 61–66 (2022).
15. Shen, P.-C. et al. Ultralow contact resistance between semimetal and monolayer semiconductors. *Nature* **593**, 211–217 (2021).
16. Lee, S., Tang, A., Aloni, S. & Wong, H.-S. P. Statistical study on the Schottky barrier reduction of tunneling contacts to CVD synthesized MoS_2. *Nano Lett.* **16**, 276–281 (2016).
17. Greiner, M. T. & Lu, Z-H. Thin-film metal oxides in organic semiconductor devices: Their electronic structures, work functions and interfaces. *NPG Asia Mater*. **5**, e55 (2013).

18. Vu, Q. A. et al. A high-on/off-ratio floating-gate memristor array on a flexible substrate via CVD-grown large-area 2D layer stacking. *Adv. Mater.* **29**, 1703363 (2017).
19. Ra, H.-S. et al. An asymmetry field-effect phototransistor for solving large exciton binding Energy of 2D TMDCs. *Adv. Mater*. **34**, 2107468 (2022).
20. Molas, M. R. et al. The optical response of monolayer, few-layer and bulk tungsten disulfide. *Nanoscale* **9**, 13128–13141 (2017).
21. Guo, F. et al. A nanocomposite ultraviolet photodetector based on interfacial trap-controlled charge injection. *Nat. Nanotech*. **7**, 798–802 (2012).
22. Konstantatos, G. et al. Sensitive solution-processed visible-wavelength photodetectors. *Nat. Photon*. **1**, 531–534 (2007).
23. Armin, A. et al. Thick junction broadband organic photodiodes. *Laser Photon. Rev.* **8**, 924–932 (2014).
24. Chen, Y. et al. Unipolar barrier photodetectors based on van der Waals heterostructures. *Nat. Electron.* **4**, 357–363 (2021).
25. Lee, H. S., Ahn, J., Shim, W., Im, S. & Hwang, D. K. 2D WSe_2/MoS_2 van der Waals heterojunction photodiode for visible-near infrared broadband detection. *Appl. Phys. Lett.* **113**, 163102 (2018).
26. Dai, M. et al. Ultrafast and sensitive self-powered photodetector featuring self-limited depletion region and fully depleted channel with van der Waals contacts. *ACS Nano* **14**, 9098–9106 (2020).
27. Ahn, J. et al. Near-infrared self-powered linearly polarized photodetection and digital incoherent holography using $WSe_2/ReSe_2$ van der Waals heterostructure. *ACS Nano* **15**, 17917−17925 (2021).
28. Zhang, Y. et al. High-speed transition-metal dichalcogenides based Schottky photodiodes for visible and infrared light communication. *ACS Nano* **16**, 19187−19198 (2022).
29. Zhang, N. et al. Near-infrared, self-powered and polarization-sensitive photodetector based on GeSe–$MoTe_2$ p–n Heterojunction. *Adv. Mater. Interfaces* **9**, 2200150 (2022).
30. Choi, S., Ahn, J., Ahn, I.-H., Hwang, D. K. & Park, M.-C. Integral imaging using a MoS_2 Schottky diode. *Opt. Lett.* **47**, 866–869 (2022).
31. Nassiri Nazif, K. et al. High-performance p–n junction transition metal dichalcogenide photovoltaic cells enabled by MoO_x doping and passivation. *Nano Lett.* **21**, 3443–3450 (2021).
32. Li, H.-M. et al. Ultimate thin vertical p–n junction composed of two- dimensional layered molybdenum disulfide. *Nat. Commun.* **6**, 6564 (2015).
33. Gong, Y. J. et al. Two-step growth of two-dimensional $WSe_2/MoSe_2$ heterostructures. *Nano Lett.* **15**, 6135–6141 (2015).
34. Li, M. Y. et al. Epitaxial growth of a monolayer WSe_2–MoS_2 lateral p-n junction with an atomically sharp interface. *Science* **349**, 524–528 (2015).
35. Tsai, M. L. et al. Single atomically sharp lateral monolayer p-n heterojunction solar cells with extraordinarily high power conversion efficiency. *Adv. Mater.* **29**, 1701168 (2017).
36. Duan, X. D. et al. Lateral epitaxial growth of two-dimensional layered semiconductor heterojunctions. *Nat. Nanotechnol*. **9**, 1024–1030 (2014).
37. Furchi, M. M., Pospischil, A., Libisch, F., Burgdörfer, J. & Mueller, T. Photovoltaic effect

in an electrically tunable van der Waals heterojunction. *Nano Lett.* **14**, 4785–4791 (2014).
38. Wong, J. et al. High photovoltaic quantum efficiency in ultrathin van der Waals heterostructures. *ACS Nano* **11**, 7230–7240 (2017).
39. Zeng, P. et al. MoS_2/WSe_2 vdW heterostructures decorated with PbS quantum dots for the development of high-performance photovoltaic and broadband photodiodes. *ACS Nano* **16**, 9329–9338 (2022).
40. Wu, F. et al. High efficiency and fast van der Waals hetero-photodiodes with a unilateral depletion region. *Nat. Commun.* **10**, 4663 (2019).
41. Went, C. M. et al. A new metal transfer process for van der Waals contacts to vertical Schottky-junction transition metal dichalcogenide photovoltaics. *Sci. Adv.* **5**, eaax6061 (2019).
42. Shanmugam, M., Bansal, T., Durcan, C. A. & Yu, B. Schottky-barrier solar cell based on layered semiconductor tungsten disulfide nanofilm. *Appl. Phys. Lett.* **101**, 263902 (2012).
43. McVay, E., Zubair, A., Lin, Y., Nourbakhsh, A. & Palacios, T. Impact of Al_2O_3 passivation on the photovoltaic performance of vertical WSe_2 Schottky junction solar cells. *ACS Appl. Mater. Interfaces* **12**, 57987–57995 (2020).
44. Kim, K.-H. et al. High-efficiency WSe_2 photovoltaic devices with electron-selective contacts. *ACS Nano* **16**, 8827–8836 (2022).
45. Nassiri Nazif, K. et al. High-specific-power flexible transition metal dichalcogenide solar cells. *Nat. Commun.* **12**, 7034 (2021).
46. Wang, H. et al. Approaching the external quantum efficiency limit in 2D photovoltaic devices. *Adv. Mater.* **34**, 2206122 (2022).
47. Georgiou, T. et al. Vertical field-effect transistor based on graphene–WS_2 heterostructures for flexible and transparent electronics. *Nat. Nanotechnol.* **8**, 100–103 (2013).
48. Guo, Y. & Robertson, J. Band engineering in transition metal dichalcogenides: stacked versus lateral heterostructures. *Appl. Phys. Lett*. **108**, 233104 (2016).
49. Xiao, W.-Z. et al. Two-dimensional H-$TiO_2/MoS_2(WS_2)$ van der Waals heterostructures for visible-light photocatalysis and energy conversion. *Appl. Surf. Sci.* **504**, 144425 (2020).